Richtmyer–Meshkov instability of a liquid–gas interface driven by a cylindrical imploding pressure wave

CrossMark

Victoria Suponitsky *, Aaron Froese, Sandra Barsky

General Fusion Inc., 108-3680 Bonneville Place, Burnaby, BC V3N 4T5, Canada

A B S T R A C T

The compression of a cylindrical gas bubble by an imploding molten lead (Pb) shell may be accompanied by the development of the Richtmyer–Meshkov (RM) instability at the liquid–gas interface due to the initial imperfection of the interface. A converging pressure wave impinging upon the interface causes a shell of liquid to detach and continue to travel inwards, compressing the gas bubble. The efficiency of compression and collapse evolution can be affected by development of the RM instability. Investigations have been performed in the regime of extreme Atwood number $A = -1$ with the additional complexity of modeling liquid cavitation in the working fluid. Simulations have been carried out using the open source CFD software OpenFOAM on a set of parameters relevant to the prototype compression system under development at General Fusion Inc. for use as a Magnetized Target Fusion (MTF) driver.

After validating the numerical setup in planar geometry, simulations have been carried out in 2D cylindrical geometry for both initially smooth and perturbed interfaces. Where possible, results have been validated against existing theoretical models and very good agreement has been found. While our main focus is on the effects of initial perturbation amplitude and azimuthal mode number, we also address differences between this problem and those usually considered, such as RM instability at an interface between two gases with a moderate density ratio. One important difference is the formation of narrow molten lead jets rapidly propagating inwards during the final stages of the collapse. Jet behavior has been observed for a range of azimuthal mode numbers and perturbation amplitudes.

© 2013 Elsevier Ltd. All rights reserved.

1. Introduction

When the interface between two fluids of different densities is subjected to rapid acceleration, e.g. by a shock passing through the interface, perturbations present at the interface prior to the passage of the wave grow with time. This phenomenon is known as the Richtmyer–Meshkov instability (RM) [1,2], and has been extensively studied in the last couple of decades. Research into the effects of the RM instability has been motivated by its relevance to astrophysics applications such as core collapse supernovae, and thermonuclear fusion applications such as inertial confinement fusion (ICF) and, more recently, magnetized target fusion (MTF).

In this paper we study the cylindrical collapse (compression) of a gas cavity by an imploding liquid shell. We focus on the RM instability [1,2], which is the first instability to develop on the liquid–gas interface during collapse. This study is motivated by the ongoing development of a prototype MTF driver at General Fusion Inc. [3,4] and primarily aimed to clarify requirements for the smoothness of the initial liquid–gas interface necessary to achieve efficient compression. In General Fusion's design,

deuterium–tritium fuel is supplied as a pair of magnetized plasma rings, known as compact toroids (CTs). The CTs are delivered to an evacuated cylindrical cavity inside a steel vessel filled with liquid lead–lithium eutectic metal and then compressed to thermonuclear fusion conditions by a converging pressure wave initiated by pneumatic pistons. Liquid Pb–17Li is used because it has several beneficial properties such a low melting point, low vapor pressure, the ability to breed tritium, a high density, which provides for a long inertial dwell time, and a good acoustic impedance match to steel, which is important for maximizing energy transfer from the steel pistons. An evacuated cylindrical cavity is formed as a result of vortical flow inside the vessel created by the tangential pumping of the liquid metal. The acoustic pulse (pressure wave) is generated mechanically by hundreds of pneumatically-driven pistons striking the outer surface of the steel vessel. The pressure wave propagates radially inwards, strengthened by a geometric convergence factor determined by the specific shape of the vessel, piston arrangement and timing. As the pressure wave reaches the liquid–plasma interface, the interface undergoes rapid acceleration and travels towards the center, compressing the plasma cavity. Perturbations existing at the liquid–gas interface prior to the passage of the pressure wave may seed the development of hydrodynamic instabilities and affect the compression efficiency. In this

* Corresponding author.
  E-mail address: victoria.suponitsky@generalfusion.com (V. Suponitsky).

study we consider compression of the cavity filled with gas (air or argon) instead of magnetized plasma by omitting the effect of the magnetic field. Magnetic stress only becomes important at the late stages of the compression and is currently under investigation. The parameters used in this study, such as size of the cavity, size of the vessel and pressure wave characteristics have been chosen to match our prototype device.

The growth characteristics of initially small-amplitude sinusoidal perturbations can be divided into two regimes: (i) the linear regime, in which the contribution of nonlinear effects is negligible and evolution of the disturbance can be adequately described by the linearized equations, and (ii) the nonlinear regime, in which the perturbation growth decreases and finally saturates due to nonlinear effects. In the linear regime, initial perturbation growth can be reasonably predicted by the simple impulse models [1,2] as $\dot{h} = h_0 A \Delta U$, where h_0 is the initial perturbation amplitude, ΔU is the difference in the velocity of the interface before and after the passage of the shock wave, and A is the Atwood number defined as

$$A = (\rho_2 - \rho_1)/(\rho_2 + \rho_1), \qquad (1)$$

where ρ_1 and ρ_2 are the fluid densities.

In literature, a characteristic pattern of RM instability is usually described in terms of fingers of one fluid penetrating into another. A finger of light fluid poking into heavy fluid is usually called a 'bubble', and that of heavy into light is called a 'spike'. Bubbles and spikes grow at the same rate during the linear stage. However during the nonlinear stage, spikes undergo acceleration whereas bubbles tend to stagnate. The disparity in growth rates becomes more prominent at high Atwood numbers ($A \approx 1$), see e.g. Dimonte and Ramaprabhu [5], and in this regime a vast majority of the existing models perform rather poorly.

Once the passing shock wave and the interface begin to interact, the evolution of the initially perturbed interface can be explained in terms of vorticity deposition. If the interface is perturbed, the pressure gradient of the shock is misaligned with the density gradient across the interface. This results in generation of the baroclinic vorticity through the term $\nabla \rho \times \nabla p$ in the vorticity equation. The sign of the generated vorticity (clockwise or counter clockwise) depends on the sign of the Atwood number, i.e. whether the shock travels from light fluid to heavy or vice versa [6,7]. As such, the initial perturbation may grow monotonically or first decrease and then grow in the opposite direction, a phenomenon known as phase inversion [8,7].

Most of the work to date on the RM instability has been carried out in rectangular geometry, with fluids modeled as ideal gases, and at moderate Atwood numbers ($|A| \approx 0.5 - 0.8$). A lot of effort was put into understanding the underlying physics, developing models describing nonlinear stages of disturbance evolution, and investigating the effects of compressibility, sensitivity to the initial conditions, and turbulent mixing, e.g. [9,10,6,11,5,12–14]. Recently, there has been an increase in the number of works describing the RM instability in converging geometries [8,15–19], which are more relevant to fusion. The situation in converging geometries is more complex than in the planar case, because the trajectories of bubbles and spikes are no longer parallel as the interface moves in the radial direction. The evolution of small- amplitude perturbations in cylindrical geometry was investigated by Mikaelian [18] for the case of pure azimuthal perturbations. Lombardini [19] extended the analysis [18] to also account for axial perturbations.

In converging geometries a fair bit of attention is devoted to the secondary effects, such as so-called 'reshock' [8,16,20–22]. In planar geometry 'reshock' has been studied by [11]. In a converging geometry the transmitted part of the shock travels to the origin, which acts as a singular point, and then bounces back to hit the interface again affecting the perturbation growth; this phenomenon is called 'reshock'.

One of the aspects of the RM instability that has been given little attention until recently is the regime of high Atwood number ($A \approx \pm 1$). This situation occurs when a shock wave passes, for example, between a liquid and a gas. In this case, at least one of the fluids cannot be described as an ideal gas and other equations of state must be considered. If one of the fluids is a liquid and the shock reflects off the interface, cavitation can occur when the pressure falls below the tensile strength of the liquid, further increasing the complexity of the problem. A recent numerical study of Ward and Pullin [23] looks into the role that the equation of state has on RM instability growth in a planar geometry. An experimental study by Buttler et al. [24] investigates the RM instability at metal-vacuum interfaces in planar geometry. Their focus was on developing an ejecta source term model that links to the surface perturbations of shocked materials. The main assumption of their model is that ejecta formation at a metal-vacuum interface can be viewed as a special limiting case of the RM instability.

Our numerical work focuses on the RM instability at a liquid–gas interface during a heavy-to-light implosion in cylindrical geometry. In this case, we have liquid Pb surrounding a cylindrical cavity of air. The pressure pulse originates in the liquid and converges toward the liquid–gas interface. When a shock wave strikes the interface between two fluids, it is partially transmitted into the second fluid and partially reflected. The transmission ratio depends on the acoustic impedance of each fluid, defined as:

$$z = \rho c, \qquad (2)$$

where ρ and c are the density and sound speed of the fluid, respectively. Therefore, the pressure pulse is almost entirely reflected when it reaches the interface because of the severe mismatch between the acoustic impedance of liquid Pb and that of air. In this configuration, the reflected wave is a rarefaction wave that subjects the liquid to tension, which may cause cavitation.

The rest of this article is organized as follows. The problem statement, numerical method and validation test are described in Section 2. The results are presented in Section 3, where pulse propagation in liquid Pb and collapse of the unperturbed cylindrical gas cavity are discussed in Section 3.1 and results for collapse of the perturbed interface are given in Section 3.2, which is further subdivided into subsections Section 3.2.1, Section 3.2.2 and Section 3.2.3 addressing effects of perturbation amplitude, azimuthal mode and comparison with theoretical models, respectively.

2. Problem statement and validation

2.1. Numerical setup

Simulations are performed using the 'compressibleInterFoam' solver, which is part of the open source C++ libraries of OpenFOAM [25]. OpenFOAM is designed to solve a generic set of partial differential equations using a finite volume computational method [26]. 'compressibleInterFoam' is a multiphase solver which uses a VOF (Volume of Fluid) phase-fraction-based interface-capturing approach and is suitable for modeling two compressible, isothermal, immiscible fluids. The momentum and other fluid properties are of the "mixture", i.e. properties vary according to the volume fraction of each phase, and a single momentum equation is solved. Governing equations are listed and discussed in Appendix A, where particular attention is given to the specific form of the equation describing evolution of the liquid fraction used in the solver.

The solver employs finite volume discretization on collocated grids such that the flow variables are cell centered, but their face-interpolated values are also used in the solution procedure.

Equations are solved through a segregated approach using the Pressure Implicit with Splitting of Operators (PISO) [27] procedure for pressure correction. The settings used in this study ensure a numerical scheme that is a second-order accurate in space and first-order accurate in time (implicit Euler).

A barotropic equation of state is used to relate pressure and density for each phase:

$$\rho_i = \rho_{0_i} + \psi_i P, \qquad (3)$$

where $\psi_i = 1/c_i^2$ is the compressibility and c_i is the speed of sound for phase i. For a gas (compressible) phase the nominal density ρ_0 in Eq. (3) is set to zero. This results in an ideal gas equation of state for an isothermal fluid. For a liquid (low compressibility phase) ρ_0 is set to the nominal density of the liquid under normal conditions. As such the fluid density remains essentially constant unless the liquid is subjected to very high pressures. Similar results can also be obtained using the Tait [28] equation of state for a liquid phase.

Simulations are carried out in 2D cylindrical geometry. A schematic of the numerical setup is shown in Fig. 1(a). The initial radius of the gas cavity and initial position of the interface is $R_0 = 0.2$ m. The outer boundary is at $R_{outer} = 1.5$ m, where a pressure pulse is imposed as a time-dependent pressure boundary condition $P(t)$ (Fig. 1(b)). The maximum pressure and duration of the pulse are chosen to reflect the parameters of the prototype device, $P_{max} = 1.5$ GPa and $T_{pulse} \approx 100$ μs in most simulations. In our prototype system characteristics of the pressure wave transferred into a molten lead depend on the velocity and design of our pneumatic pistons. A realistic shape (spatial and temporal) of the pulse is complex as it involves propagation of the pulse along the piston and interaction with the surrounding steel. A simplified pulse shown in Fig. 1(b) has been chosen to reflect a maximum pressure, expected duration and initial ramp rate of the pulse. It is based on the results of FEA structural simulations performed with the commercial software LS-DYNA [29]. It should be noted that as the initial pulse propagates through the molten lead towards the gas cavity, its shape and amplitude change. The front becomes steeper and the rear end becomes longer leading to the shortening of the flat portion; the pulse shape becomes more triangular as it propagates. The peak amplitude of the pulse also undergoes amplification because of the converging geometry.
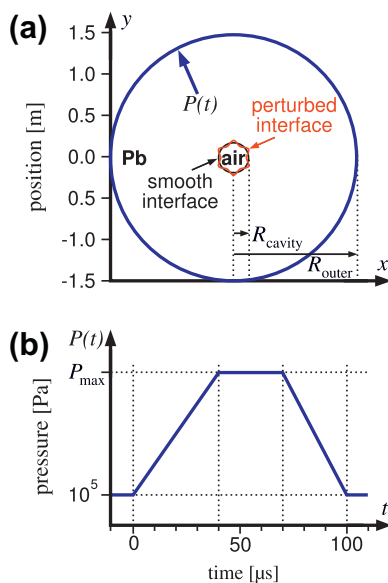

Fig. 1. (a) Numerical setup for 2D simulations in a cylindrical geometry. (b) Typical shape of the pressure pulse imposed on the outer boundary.

A zero-gradient boundary condition is set for the velocity at the outer boundary allowing some mass influx into the domain. In most simulations a small central portion of the computational domain with radius $r < 1$ cm has been excluded from the calculations to speed up the computations. The effect of excluding this central part was found to be negligible for the purposes of this work. The inner boundary uses an outflow boundary condition so that gas can 'escape' from the domain during the collapse. Both fluids are initially at rest at atmospheric pressure.

Simulations are carried out for both initially smooth and sinusoidally perturbed interfaces. The results for the unperturbed case are first validated against existing models and then used as a baseline of comparison for the growth of bubbles and spikes in perturbed interface runs. The initial sinusoidal perturbation is defined by its initial amplitude h_0 and azimuthal mode wavenumber n, with a corresponding perturbation wavelength of $\lambda_0 = 2\pi R_0/n$. The perturbation amplitude can be normalized relative to its wavelength, h_0/λ_0, as is done in planar geometry, or relative to the initial radius of the interface h_0/R_0, which indicates how much the behavior is affected by the curvature of the interface.

Simulations with a coarse grid resolution in the radial direction ($\hat{r}$) are performed over the full azimuthal domain (Fig. 1(a)), while finer grid resolution runs are carried out over a restricted azimuthal angle $\theta_{segment}$ (with periodic boundary conditions in the azimuthal direction) to speed up the calculations. The specific choice of $\theta_{segment}$ depends on the azimuthal mode number n of the perturbation used. The number of grid points in the radial direction is $N_r = 2800$ and $N_r = 11,200$ for the coarse and fine resolution runs, respectively. The grid spacing is uniform for $r < R_0$ with $dr = 2.375 \times 10^{-4}$ m and $dr = 5.9375 \times 10^{-5}$ m for the coarse and fine grids, respectively. The smallest perturbation amplitude used in these simulations is $h_0 = 0.001$ m. This results in 17 fine grid points across the initial perturbation in the radial direction. The number of grid points per perturbation wavelength is set to $N_\theta = 135$ in most simulations, although this is reduced to $N_\theta = 55$ for high azimuthal mode perturbations.

Simulations are performed for an implosion of molten lead Pb into air with the fluid properties $\rho_{Pb} = 10,000$ kg/m³, $c_{Pb} = 2000$ m/s; $\rho_{air} = 1$ kg/m³, $c_{air} = 316$ m/s. Properties of the molten Pb at 400 °C were taken from [30], although a value of sound speed was rounded from 1800 m/s to 2000 m/s for analytic simplicity. The corresponding acoustic impedances (Eq. (2)) are $z_{Pb} = 2 \times 10^7$ Rayl and $z_{air} = 316$ Rayl and the Atwood number is $A = (\rho_{air} - \rho_{Pb})/(\rho_{air} + \rho_{Pb}) = -0.9998 \approx -1$.

Finally, we should note that by using the isothermal fluids assumption, we do not take into account that some energy of the pressure pulse is converted into heat as the pulse propagates through the molten lead. The isothermal assumption is also inaccurate for adequate description of gas pressurization. However, the gas has very little effect on the molten Pb until the very last stage of compression, when gas pressure becomes comparable to the pressure of the liquid shell (deceleration phase), which we do not concern ourselves about in this study. Both the gas pressure and magnetic stress provide the mechanism to decelerate the liquid shell, but they are beyond scope of this study. Rotation of the fluid has not been included in this study as well.

2.2. Validation test

The numerical method and grid convergence are first tested in planar geometry on a set of parameters similar to those used in cylindrical geometry. The length of the computational domain in the streamwise direction ($\hat{x}$, normal to the interface) is $L_x = 1.5$ m with the interface located at $X_{interface} = 1.3$ m. A pressure pulse $P(t)$ is prescribed at the inflow boundary at $X = 0$ and an outflow

(zero-gradient) boundary condition is used at $X = 1.5$ m. The initial pressure pulse amplitude is $P_{max} = 3.6$ GPa which roughly corresponds to the expected pressure at the interface in cylindrical geometry when the initial pulse amplitude is $P_{max} = 1.5$ GPa and pressure is amplified due to the convergence. In the normal direction ($\hat{y}$, parallel to the surface of the interface) the length of the computational domain is one wavelength of a mode $n = 6$ perturbation of cylindrical geometry, $L_y = 2\pi R_0/n = 0.2094395102$ m. Periodic boundary conditions are imposed in the normal direction and the number of grid points is set to be $N_y = 135$, corresponding to the $n = 6$ case in cylindrical geometry. Simulations are performed for three different grid resolutions in the streamwise direction. The grid spacing is uniform for 1.3 m $\leqslant X \leqslant 1.5$ m and equal to $\Delta x = 2.375 \times 10^{-4}$, 1.1875×10^{-4} and 5.9375×10^{-5} m for grids with increasing resolution. The total number of grid points in the streamwise direction is correspondingly $N_x = 2800, 5600$ and 11200.

A schematic of the flow pattern in the planar case is shown in Fig. 2. Part (a) of the figure shows propagation of the pressure pulse through Pb prior to hitting the interface and part (b) illustrates the flow pattern some time after the pressure pulse hits the interface. The pressure pulse gets reflected from the interface as a rarefaction wave. This puts the liquid Pb into tension and initiates cavitation behind the interface (Fig. 2(b)).

In planar geometry, an initially smooth interface is expected to move with constant velocity after interacting with the pressure pulse. In our case, the interface velocity $V_{\text{interface}}$ can be approximated by assuming two fluids with a very large impedance ratio (see Section 4.8 and Section 4.9 in [31]), such that,

$$V_{\text{interface}} \approx 2V_p, \tag{4}$$

where V_p is the particle velocity given by,

$$V_p = \frac{P_{max} - P_0}{\rho_{Pb}c_{Pb}} \approx \frac{P_{max}}{\rho_{Pb}c_{Pb}}. \tag{5}$$

The maximum pressure P_{max} and density ρ_{Pb} of the pulse are taken just before it hits the interface. The ambient pressure is $P_0 = 1 \times 10^5$ Pa. It should be noted that Eq. (4) is strictly valid for a shock wave. Our initial ramped pressure pulse steepens during its propagation and becomes a shock before hitting the interface
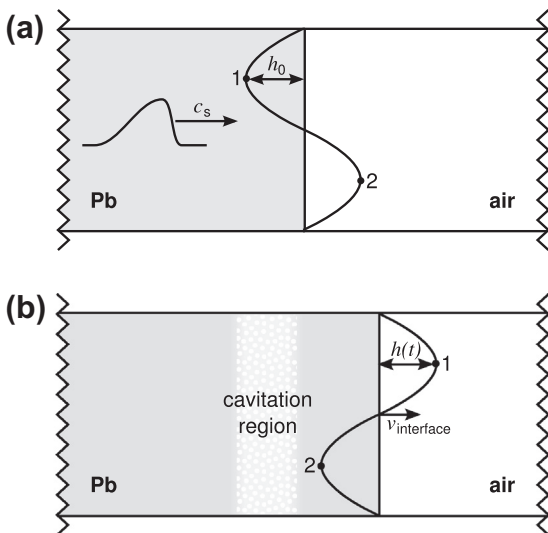
(see Fig. 5 at $t = 650$ μs). As such, we expect our results to be in a good agreement with Eq. (4).

The evolution of an initially smooth interface after it has been accelerated by a linearly ramped pressure pulse of infinite length is shown in Fig. 3 for two different grid resolutions. One can see that the grid resolution is sufficient to obtain well converged results. For our parameters, $P_{max} \approx 3.6$ GPa, $\rho_{Pb} \approx 10,500$ kg/m^3 (there is a slight increase in Pb density as the pulse propagates through it due to compressibility) and $c_{Pb} \approx 2000$ m/s, the interface velocity predicted by Eq. (4) is $V_{\text{interface}} = 343$ m/s. The numerically calculated velocity (slope of the curve) is $U_{\text{interface}} = 344.7$ m/s, which deviates from the theoretical value by less than 0.5%.

An initially perturbed interface is also tested in planar geometry. The initial perturbation amplitude is set to $h_0 = 2$ mm (Fig. 2) and the perturbation wavelength λ_0 is equal to the length of the computational domain in the normal direction $\hat{y}$ leading to $h_0/\lambda_0 = 9.55 \times 10^{-3}$. In our analysis we follow the extrema points of the perturbations, marked by points 1 and 2 in Fig. 2, which we label, respectively, as bubbles and spikes throughout the entire simulation. It is important to note that during the first stage of the compression phase inversion [8] occurs. This means that the perturbation which is initially a spike, i.e. heavy fluid surrounded by light fluid, reverses to become a bubble and vice versa. As such our label 'spike' corresponds to a finger of a heavy fluid surrounded by light fluid once the phase inversion has occurred, whereas at early stages it is a finger of light fluid surrounded by heavy. The converse applies to bubbles.

Early evolution of the normalized spike amplitude is shown in Fig. 4 for pressure pulses of different duration, each with a maximum pressure of $P_{max} = 3.6$ GPa and modeled at the finest grid resolution. The spike amplitude has been calculated as the difference between the interface position at point 1 for the case of a perturbed interface and the coincidental position of the initially unperturbed interface. One can see that for longer pulses ($T_{\text{pulse}} \geqslant 200$ μs) the pulse length has no effect on the spike amplitude. However, if the pulse length falls below some threshold, the spikes' amplitude growth slows down, clearly seen by comparing results in Fig. 4 for the shortest pulse $T_{\text{pulse}} = 100$ μs (red line) with those obtained for longer pulses.

Initial disturbance growth rates (indicated by the slope of the curves in Fig. 4) together with the growth rate predicted by the Richtmyer impulsive model [1] (given below by Eq. (6)) for our set of parameters are listed in Table 1.

$$\dot{h}_{\text{planar}} = h_0^+ k A^+ \Delta U, \tag{6}$$

where $k = 2\pi/\lambda$ is the wave number of the perturbation, h_0^+ and A^+ are the initial post-shock amplitude and Atwood number, and ΔU is

Fig. 2. Schematic of a test case in planar geometry. (a) Pressure pulse propages through Pb prior to hitting the Pb–air interface. (b) Some time after the pressure pulse hits the Pb–air interface. Pb shell is formed and a phase inversion occurs on the perturbed interface.
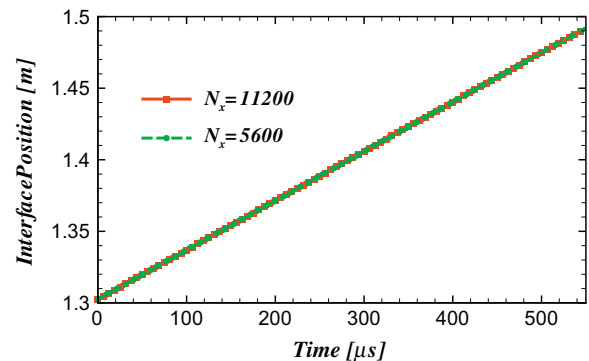

Fig. 3. Planar geometry: evolution of the initially smooth interface for two grid resolutions. Pressure pulse is of an infinite length and amplitude $P_{max} = 3.6$ GPa.
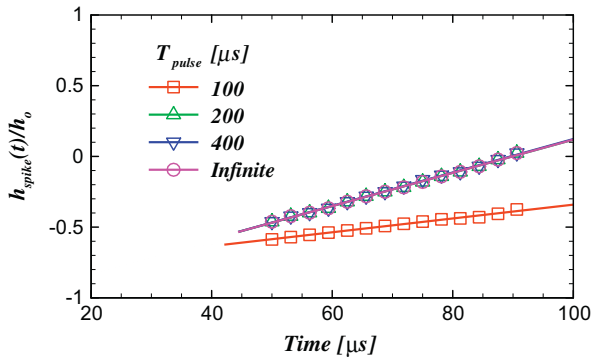
Fig. 4. Planar geometry: early evolution of the normalized spike amplitude for pressure pulses with various lengths. Maximum pulse pressure is $P_{max} = 3.6$ GPa and initial perturbation amplitude is $h_0/\lambda = 9.55 \times 10^{-3}$.

Table 1
Planar case: initial growth rate.

Case	h_0 (m)	T_{pulse} (µs)	$\dot{h}$ (m/s)
Richtmyer model [1] (Eq. (6))	0.002	Infinite	20.7
OpenFOAM simulation	0.002	Infinite	23.0
OpenFOAM simulation	0.002	100	9.8

the velocity jump at the interface following passage of the shock. In our validation case we use $k = 30, h_0^+ = 2$ mm, $A^+ = 1$, and $\Delta U = V_{interface} = 345$ m/s, resulting in $\dot{h} \approx 20.7$ m/s (see Table 1). Our results for longer pulses agree well with the Richtmyer impulsive model, while for a shorter pulse the growth rate is lower.

Propagation of the pressure pulse through Pb for the validation case discussed above is shown in Fig. 5 for pulses with $T_{pulse} = 100$ and 200 µs. Contours of the liquid phase fraction are shown in Fig. 6, where part (a) shows the initial perturbation with amplitude $ho = 2$ mm, parts (b) and (c) show the flow field obtained for pulses with $T_{pulse} = 100$ and 200 µs at $t = 450$ µs from the moment the pressure pulse hits the interface, and for a sake of completeness, part (d) shows the flow field obtained in the case of the initially unperturbed interface for the pressure pulse $T_{pulse} = 100$ µs at $t = 450$ µs. It can be seen that as a pulse propagates through the Pb its amplitude remains constant (as expected in a planar geometry), but its shape changes; the front steepens and the back decays. We can also see that the short pulse has a triangular shape when it reaches the interface, unlike longer pulses that still have a considerable 'flat' section. This difference in the pulse shape is a
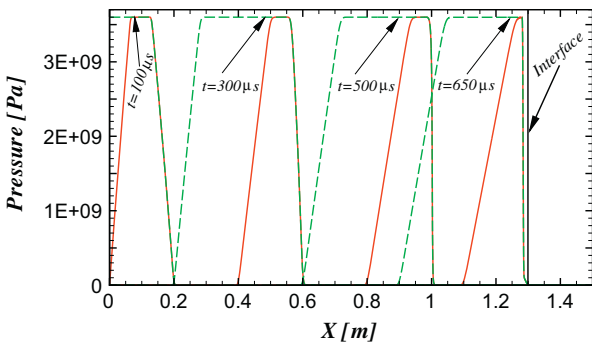

Fig. 5. Planar geometry: pressure pulse propagation from $X = 0$ towards the interface at $X = 1.3$ m. Initial pulse amplitude is $P_{max} = 3.6$ GPa and pulse duration is $T_{pulse} = 100$ µs (red solid line) and $T_{pulse} = 200$ µs (green broken line). (For interpretation of the references to color in this figure legend, the reader is referred to the web version of this article.)
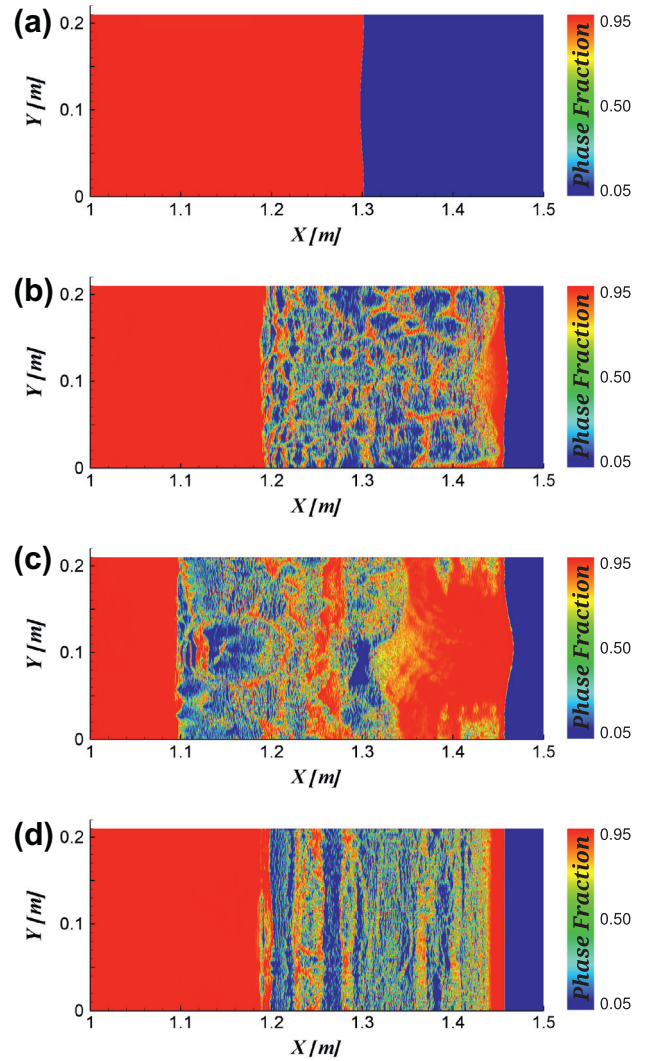

Fig. 6. Planar geometry: liquid phase fraction contours (a) initial perturbation with $h_o = 2$ mm; (b) flow field at $t = 450$ µs (taken from the moment pressure pulse hits the interface) for $T_{pulse} = 100$ µs; (c) flow field at $t = 450$ µs for $T_{pulse} = 200$ µs; (d) flow field at $t = 450$ µs for initially unperturbed interface and pulse duration $T_{pulse} = 100$ µs.

likely reason for the difference in the perturbation growth rates obtained for a short ($T_{pulse} = 100$ µs) and longer ($T_{pulse} \geqslant 200$ µs) pulses (see Table 1), as *RM* instability growth rates are known to be sensitive to the initial conditions.

A higher perturbation amplitude in the case of the longer pulse is also evident from Fig. 6 by comparing parts (b) and (c) of the figure. One can see that while the overall structure of the flow remains similar for pulses of different duration, the thickness of the spalled layer varies. This is also due to the difference in the pressure pulse shape proximal to the interface.

3. Results

3.1. Pulse propagation and gas cavity collapse: unperturbed interface

In this section we study the collapse of an initially unperturbed gas cavity in 2D cylindrical geometry. The numerical results are validated against existing theoretical models and also used as a baseline for calculations of the perturbation growth for the runs with initially perturbed interfaces.
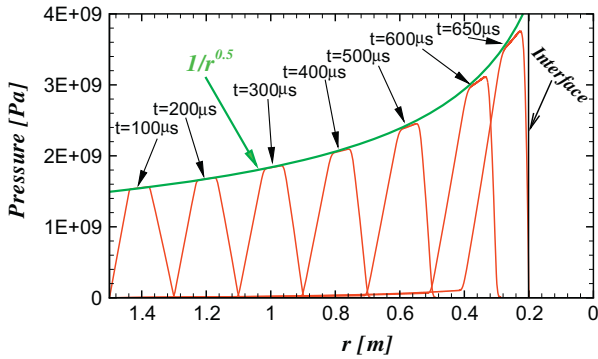
Fig. 7. Pressure pulse propagation from the outer boundary at $r = 1.5$ m towards the interface at $r = 0.2$ m in cylindrical geometry. Initial pulse amplitude is $P_{max} = 1.5$ GPa and pulse duration is $T_{pulse} = 100$ µs. The pulse propagates from left to right.

Propagation of a pressure pulse through the liquid Pb from the outer boundary towards the interface in a cylindrical geometry is shown in Fig. 7. The pressure pulse has a maximum initial amplitude of $P_{max} = 1.5$ GPa and duration $T_{pulse} = 100$ µs. It can be seen that the pressure pulse is amplified as it cylindrically converges in the Pb. This amplification is in excellent agreement with the theoretical prediction that a small-amplitude (linear) pulse grows like $P \sim 1/\sqrt{r}$ in cylindrical geometry [32]. (The pulse is expected to exhibit linear behavior when the particle velocity is much less than the sound speed.) As the pulse approaches the interface and pressure becomes higher, nonlinearity starts to manifest itself by a steepening of the pulse front and a slight deviation of the amplitude from the theoretical curve. For the parameters near the interface ($P_{max} \approx 3.6$ GPa, $\rho_{Pb} \approx 10,500$ kg/m³ and $c_{Pb} \approx 2000$ m/s) the particle velocity can be roughly estimated as $V_p \approx 171$ m/s by Eq. (5). This velocity is still relatively small (but not negligible) compared to the speed of sound (171 m/s compared to 2000 m/s). Thus the pulse exhibits predominantly linear behavior as it propagates through the Pb, although small nonlinear effects become noticeable near the interface. The time taken for the pulse to reach the interface 1.3 m away is $t_{propagation} = 650$ µs, which agrees with the prescribed speed of sound $c_{Pb} = 2000$ m/s. In subsequent results, time is defined relative to the moment the pressure pulse reaches the interface, such that $t = t_{sim} - t_{propagation}$.

A typical structure of the flow field during the collapse of an initially unperturbed cylindrical cavity is shown in Fig. 8 for a pressure pulse of duration $T_{pulse} = 100$ µs and maximum pressure $P_{max} = 1.5$ GPa. Parts (a) and (b) of the figure show liquid phase fraction contours when the pressure pulse strikes the interface at

$t = 0$ and when the cavity has partially collapsed at $t = 300$ µs, respectively. Part (c) shows the corresponding pressure contours at $t = 300$ µs. It is worth reiterating that the imploding material is liquid Pb with an acoustic impedance much larger than the air in the cavity. Therefore, the pressure pulse is almost completely reflected back into the Pb as a rarefaction wave. The molten lead is then subjected to tension which causes it to cavitate. It is apparent in Fig. 8(b) that a Pb shell forms as a result of interaction between the pressure pulse and the liquid–gas interface. As the shell moves inwards, a cavitation region forms behind it, separating it from the rest of the molten lead. The pressure contours in Fig. 8(c) show that the Pb shell becomes pressurized as it converges, while the pressure in the cavitation region falls to the minimum allowed by the numerical setup. We should also note that for the initially unperturbed interface the inner edge of the shell (liquid–gas interface) remains smooth during the collapse, whereas some random perturbations appear on the outer edge of the shell (Figs. 8(b) and (c)). Such perturbations are likely to be numerically seeded as cavitation layers being formed in molten Pb. The shell formed in this example is of a sufficient thickness that those perturbations do not impact the inner edge of the shell and therefore they are of no concern in the current study.

Radial profiles of the pressure, velocity and liquid phase fraction at two different instances during the collapse ($t = 100$ µs and $t = 300$ µs) are shown in Fig. 9. We mainly focus on the behavior of the molten lead because dynamics of the gas bubble have very little effect on the liquid Pb until the very late stages of the collapse. Liquid phase fraction profiles clearly show the location of the liquid–gas interface and growth of the cavitation region (characterized by rapid oscillations in the liquid phase fraction profile) as the interface progresses inwards. Also evident is the increase in the thickness of the Pb shell as it converges during the collapse process. From the pressure profiles we can see that the shell is pressurized as it moves toward the center. The pressure in the cavitation region becomes almost zero and the pressure inside the air increases as it is compressed. Velocity profiles indicate that the velocity gradually increases towards smaller radii both in the cavitation region and the Pb shell, i.e. shell's inner edge is moving faster than its outer edge. During early stages of the collapse, the interface velocity (which is equal to the fluid velocity at the position of the interface) roughly corresponds to Eq. (4), but later increases due to the converging geometry.

If we look at the flow field structure inside the gas cavity one can observe a shock wave propagating through it. This shock wave is generated in the air due to the sudden acceleration of the interface. The interface is analogous to a piston at rest that suddenly begins moving into a quiescent gas at constant velocity. In this
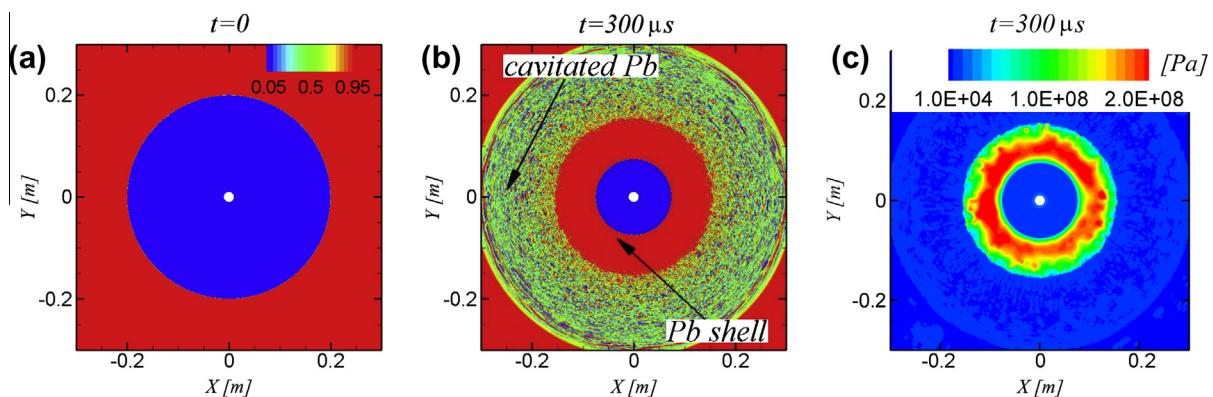

Fig. 8. Structure of the flow field during compression of initially unperturbed gas cavity by pressure pulse with $T_{pulse} = 100$ µs and $P_{max} = 1.5$ GPa. (a) Liquid phase fraction contours when the pressure pulse hits the interface; (b) liquid phase fraction contours and (c) pressure contours when the cavity has partially collapsed at $t = 300$ µs.
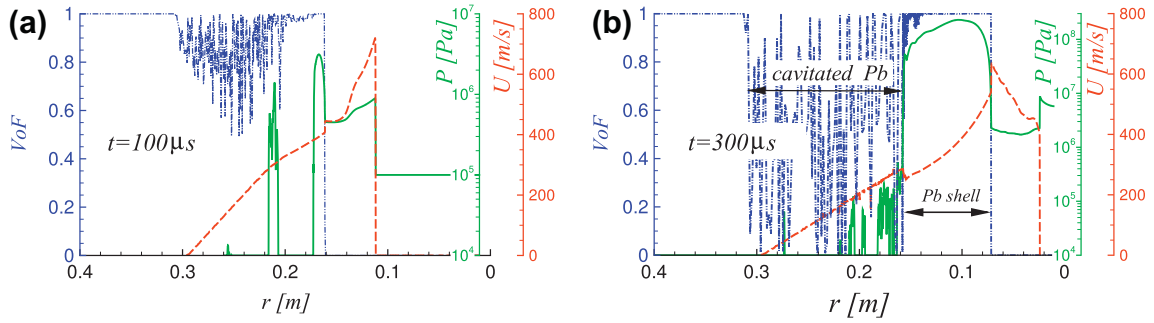
Fig. 9. Structure of the flow field during compression of initially unperturbed gas cavity by pressure pulse with $T_{pulse} = 100$ μs and $P_{max} = 1.5$ GPa. Radial profiles of liquid phase fraction (blue dash-dot line), pressure (green solid line), and velocity (red broken line) during the collapse. (a) $t = 100$ μs and (b) $t = 300$ μs. (For interpretation of the references to colour in this figure legend, the reader is referred to the web version of this article.)

situation, a shock front immediately appears, moving away from the piston with a constant supersonic speed. Ahead of the shock front the gas is at rest, while behind the shock it moves at the same velocity as the piston, i.e. the interface velocity in our case (see [33] Section 3). Note that our numerical method is not sufficient for a high-accuracy solution of shock wave propagation inside the compressed gas. However, as mentioned earlier, the gas dynamics have little effect on the collapse, so the current numerical setup is satisfactory for this study.

It is necessary to accurately predict the trajectory of the liquid–gas interface throughout the collapse so that the compression efficiency of our system can be estimated. The motion of an initially unperturbed interface in cylindrical geometry is shown in Fig. 10. The four different lines show our numerical results obtained for the pressure pulses of various durations with maximum pressure $P_{max} = 1.5$ GPa. The theoretical solution of Kedrinskii (Section 1.4 in [34]) is also shown by the black solid line for comparison. One can see that the duration of the pulse influences the collapse time; longer pulses compress the cavity faster. This effect, however, diminishes as the pulse duration is increased, such that no difference in collapse time is observed for pulses with $T_{pulse} \geqslant 400$ μs. Our results for the longer pulses are also in very good agreement with a theoretical solution developed by Kedrinskii [34]) for studying underwater explosions.[1] Some additional results concerning the effect of the pressure pulse amplitude as well as collapse characteristics of the initially unperturbed spherical cavity can be found in our earlier work [36].

It is worth noting that in the current numerical setup the gas never becomes sufficiently pressurized to affect the trajectory of the interface, which accelerates all the way to the axis due to geometrical convergence. In reality, however, the interface undergoes rapid deceleration later in the compression because the gas pressure becomes comparable to the pressure in the Pb shell. This
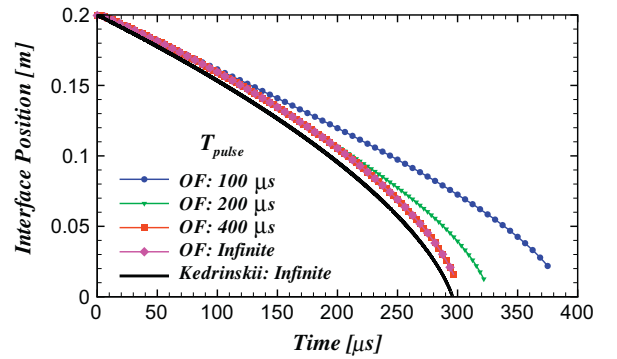
---

[1] Detonating an explosive charge underwater distributes energy between detonation products and liquid. The gas in the explosive cavity is heated and acts as a piston on the water, generating a shock wave. The Kirkwood–Bethe approach [35] to the problems of underwater explosion can be used to derive the pulsation equation, the equation of motion for the edge of the cavity. Because it applies to states after the detonation, it can also be applied to our problem of a shock impinging on a pre-existing cavity. The pulsation equation for a one-dimensional isentropic compressible liquid flow is presented by Kedrinskii [34] as

$$R\left(1 - \frac{\dot{R}}{c}\right)\ddot{R} + \frac{3}{4}v\left(1 - \frac{\dot{R}}{3c}\right)\dot{R}^2 = \frac{v}{2}\left(1 + \frac{\dot{R}}{c}\right)H + \frac{R}{c}\left(1 - \frac{\dot{R}}{c}\right)\frac{dH}{dt}, \qquad (7)$$

where R is the cavity radius, c is the local speed of sound, H is the enthalpy on the cavity wall from the liquid side, and v depends on the symmetry, which can be planar ($v = 0$), cylindrical ($v = 1$), or spherical ($v = 2$). When the pressure in the cavity is much less than the shock pressure, the enthalphy at the interface is always zero ($H = 0$), eliminating the RHS. Then the liquid collapse is determined only by geometric convergence, which can be solved numerically.

Fig. 10. Effect of pressure pulse duration T_{pulse} on motion of liquid–gas interface during collapse of initially unperturbed cylindrical cavity. Semi-analytical solution of Kedrinski [34] is also plotted as black solid line. Maximum pulse pressure is $P_{max} = 1.5$ GPa.

deceleration is very important as the interface becomes Rayleigh–Taylor unstable during this phase.

3.2. The Richtmyer–Meshkov instability

Now we turn our attention to the development of the RM instability during the collapse due to imperfections that may be present on the liquid–gas interface. In order to understand how various perturbations are going to affect the compression efficiency of our system, we study effects of the initial perturbation amplitude and azimuthal mode number. The parameters for each simulation are summarized in Table 2. In all cases, the pressure pulse has an amplitude of $P_{max} = 1.5$ GPa and a duration of $T_{pulse} = 100$ μs.

A typical perturbation evolution during the early and late stages of the collapse is shown in Figs. 11 and 12, respectively. In both figures, the liquid phase fraction contours are plotted in the first row and the corresponding contours of the $\hat{z}$ vorticity component multiplied by liquid phase fraction are plotted in the second row.[2] The position of the initially unperturbed interface is also shown by the black solid line. Results are presented for case N12A002 listed in Table 2 with an initial amplitude of $h_0 = 2$ mm and $n = 12$.

One can see that once the pressure pulse interacts with the perturbed liquid–gas interface (Fig. 11 at $t = 0$), vorticity is immediately generated in the vicinity of the interface because density and pressure gradients are initially misaligned, i.e. the mechanism

---

[2] Due to very high velocities and gradients, vorticity attains very high values in the gas, hiding what happens in the Pb. Multiplying vorticity by liquid phase fraction basically gives us vorticity contours only in the Pb, which is of greatest interest.

Table 2
List of parameters for the simulations performed.

No.	Name	n	h_0 (m)	h_0/R_0	h_0/λ_0
1	N3A001	3	0.001	0.005	0.002387
2	N4A001	4	0.001	0.005	0.003183
3	N6A001	6	0.001	0.005	0.004775
4	N8A001	8	0.001	0.005	0.006366
5	N12A001	12	0.001	0.005	0.009549
6	N12A002	12	0.002	0.010	0.019098
7	N16A001	16	0.001	0.005	0.01273
8	N24A001	24	0.001	0.005	0.01909
9	N32A001	32	0.001	0.005	0.02546
10	N6A002	6	0.002	0.010	0.009549
11	N6A004	6	0.004	0.020	0.01909
12	N6A010	6	0.010	0.050	0.04775
13	N3A004	3	0.004	0.020	0.009549
14	N3A008	3	0.008	0.040	0.01909

of baroclinic vorticity generation. For a pulse passing from a heavy fluid into a light one, the deposited vorticity initially acts in the direction opposite to that of the perturbation, smoothing the interface during the early evolution stages (Fig. 11 at $t = 44\,\mu$s). Vorticity then continues to deflect the interface leading to the growth of the perturbation in the opposite direction, i.e. phase inversion (Fig. 11 at $t = 110\,\mu$s and $t = 210\,\mu$s). The asymmetry between the spikes and bubbles observed in Fig. 11 at $t = 210\,\mu$s indicates that the perturbation is entering a nonlinear stage of evolution.

There are two nondimensional parameters that can be used to characterize evolution of the perturbation amplitude. The first one is the ratio of the perturbation amplitude and wavelength $h(t)/\lambda(t)$. Similar to the planar case, perturbation evolution is considered to be linear when $h(t)/\lambda(t) \ll 1$. However, in cylindrical geometry the wavelength of the perturbation decreases as the cavity collapces so that nonlinear effects become prominent earlier than in the planar case. The second parameter is the ratio between the disturbance amplitude and radius of the cavity $h(t)/R(t)$. This parameter indicates how much the perturbation evolution is influenced by the curvature of the interface. For small-amplitude dis-

turbances, the parameter $h(t)/R(t)$ is small. At early stages of the collapse only low azimuthal modes are expected to be influenced by the curvature of the interface as they have significant ratios of $\lambda(t)/R(t)$, whereas early evolution of the perturbations at higher azimuthal modes is expected to be similar to that of the planar case. As the cavity continues to be compressed, however, the decrease in cavity radius increases the number of modes that are affected by curvature. Therefore, while the initial motion may be negligibly different from the planar case, we expect convergence effects to manifest themselves more strongly as compression proceeds.

Keeping the above in mind we follow the spike evolution in Figs. 11 and 12. One can see that after phase inversion is complete ($t = 110$, 210, and $312.5\,\mu$s), the spike amplitude grows, i.e. the distance increases between the crest of the perturbation and the position of the initially unperturbed interface. At later stages ($t = 350$, 362.5, and $375\,\mu$s), the spike amplitude starts to decrease. This decrease in the perturbation amplitude correlates with the increase of parameter $h(t)/R(t)$. By examining the vorticity distribution, a reversal of the vorticity along the spike interface near the crest can be observed. This change in direction of rotation correlates with the direction of interface deflection, best seen by comparing times $t = 210$ and $312.5\,\mu$s. One can also see the Kelvin–Helmholtz (K–H) instability that develops on the sides of the bubbles and spikes at later times $t > 300\,\mu$s, giving them a serrated appearance.

Another interesting phenomenon that can be observed in Figs. 11 and 12 is the formation of narrow molten lead jets (ribs) originating from the head of the bubble after $t = 350\,\mu$s. Formation of such jets has been observed in our simulations for perturbations with azimuthal mode numbers higher than four ($n > 4$). The prominence of the jets is dependent on the amplitude and mode of the initial perturbation. For this example case, the narrow jets only form but do not overtake the original spikes during the collapse. Instead, the spikes grew sufficiently to contact one another near the center, despite the deceleration they experience late in the collapse.
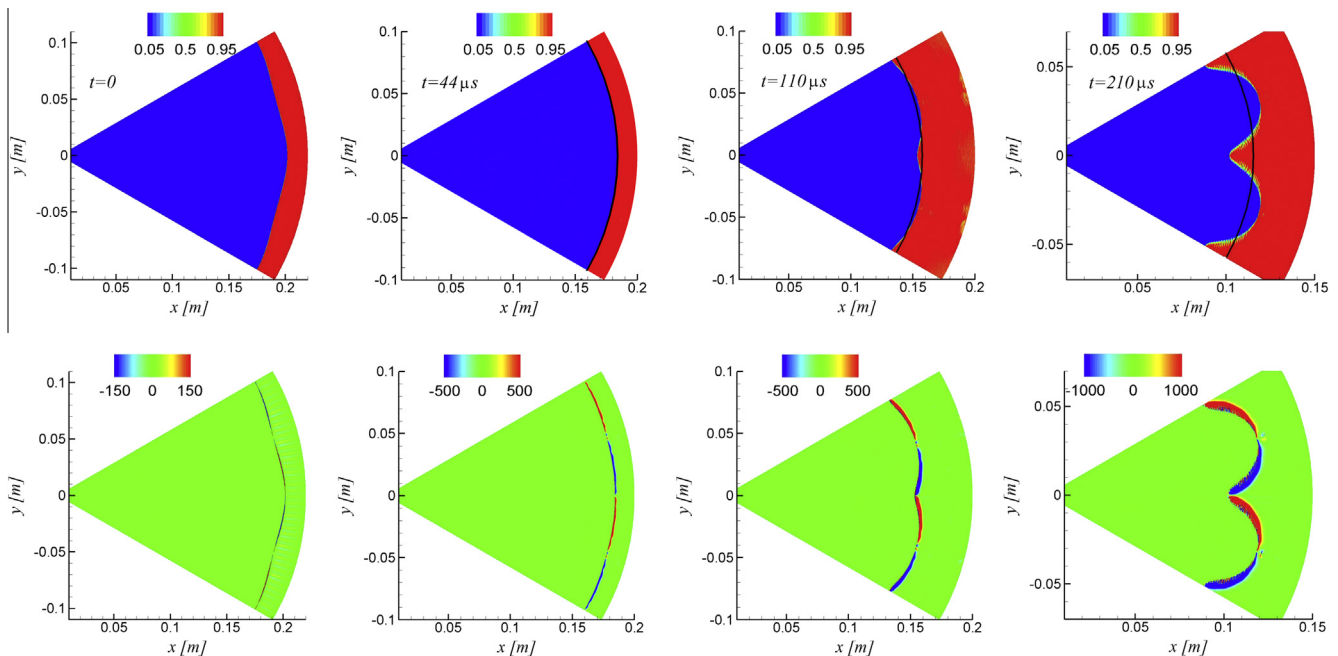

Fig. 11. Early development of RM instability shown by liquid phase fraction contours (first row) and contours of the vorticity component in $\hat{z}$ direction (units [1/s]) multiplied by liquid phase fraction (second row). Initial perturbation is at azimuthal mode $n = 12$ with amplitude of $h_0 = 2$ mm (Case N12A002 in Table 2). Black solid line shows interface position for initially unperturbed case. Pressure pulse has amplitude $P_{max} = 1.5$ GPa and duration $P_{pulse} = 100\,\mu$s.
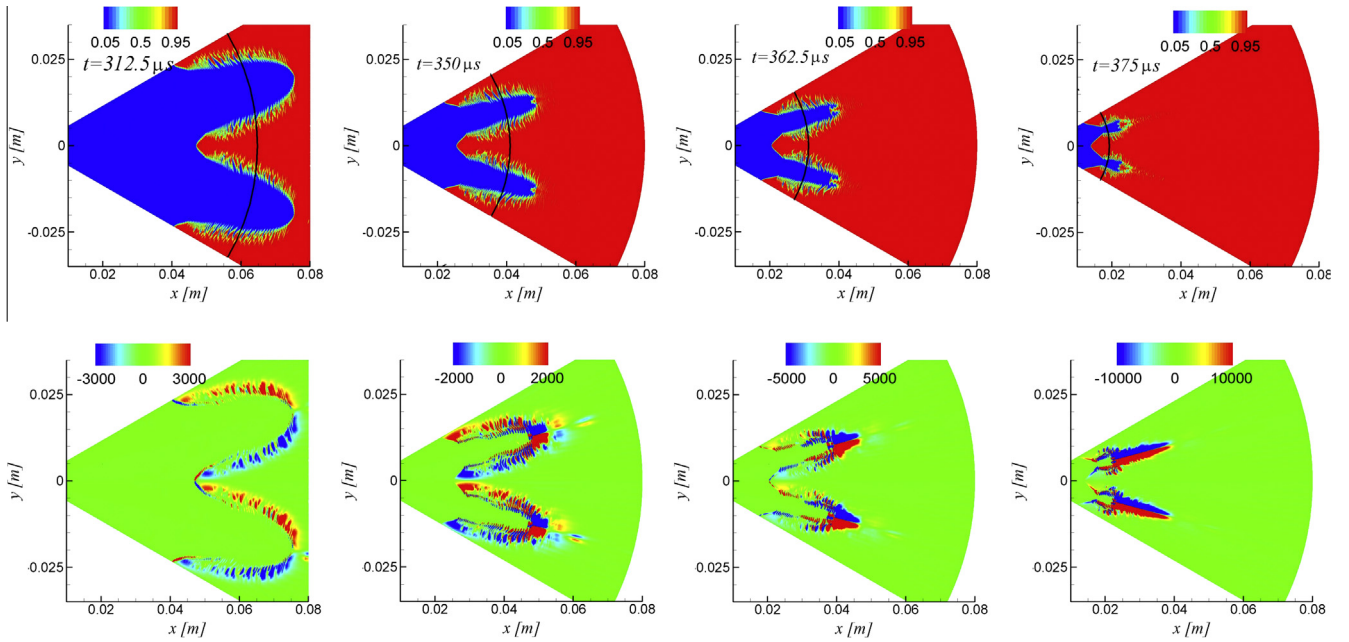
Fig. 12. Late development of RM instability shown by liquid phase fraction contours (first row) and contours of vorticity component in $\hat{z}$ direction (units $[1/s]$) multiplied by liquid phase fraction (second row). Initial perturbation is at azimuthal mode $n = 12$ with amplitude of $h_0 = 2$ mm (Case N12A002 in Table 2). Black solid line shows interface position for initially unperturbed case. Pressure pulse has amplitude $P_{max} = 1.5$ GPa and duration $P_{pulse} = 100$ μs.

For the case of a perturbation with the same mode, but a lower initial amplitude, the situation is different, as shown in Fig. 13. This figure is in the same format as Fig. 12 (first row showing liquid phase fraction contours and the second z-vorticity component multiplied by the liquid phase fraction), but for case N12A001 in Table 2, which has a lower initial amplitude of $h_0 = 1$ mm. One can see that for this smaller perturbation, amplitude decreases during the late stages of the collapse; a second phase inversion.

The reason for this kind of oscillatory behavior is discussed further in Section 3.2.3. By comparing vorticity distributions at times $t = 312.5$ and 350 μs in Fig. 13, it becomes apparent that this oscillatory behavior is accompanied by a reversal of the sign of vorticity.

With regard to the formation of the narrow molten lead jets, it can be seen that in this case they move fast enough to overtake the original spikes and reach the center first. We are not aware of such
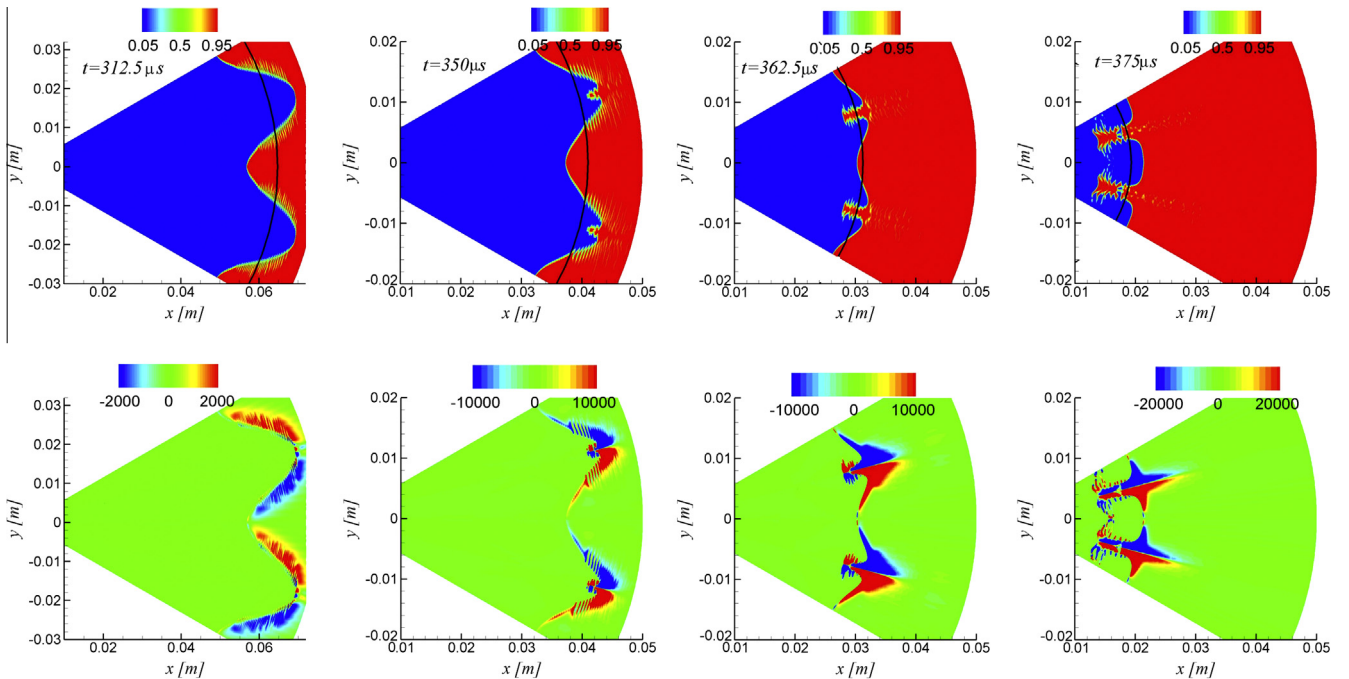

Fig. 13. Formation of rib-like jets during late stages of collapse. Liquid phase fraction contours are shown in first row. Contours of vorticity component in $\hat{z}$ direction (units $[1/s]$) multiplied by liquid phase fraction are shown in second row. Initial perturbation is mode $n = 12$ with amplitude $h_0 = 1$ mm (Case N12A001 in Table 2). Black solid line shows interface position for initially unperturbed case. Pressure pulse has amplitude $P_{max} = 1.5$ GPa and duration $T_{pulse} = 100$ μs.

jets being observed in other works that use two gases with a moderate Atwood number as the working fluids. A very similar phenomenon has been observed, however, in the recent works of Enriquez et al. [37,38]. In those works gravity-induced collapse of nonaxisymmetric air cavities created by driving a metal disc through an initially quiescent water surface has been investigated. In [37,38] a formation of ridge-like jets at the head of bubble has been observed over the range of azimuthal mode numbers and amplitudes of the initial perturbation (see for example Fig. 1 in [37] and Fig.11 in [38] for perturbation at $n = 6$). Formation of such jets at low azimuthal modes ($n \leqslant 4$) has not been observed in [37,38] which fully agrees with our results. The narrow jets are ob-

served to form in experiment when the bubble structure becomes pointy at some moment during the nonlinear stage. The jets originate in singular cusps where the flow converges.

Examining our results (Fig. 13) we can see that: (i) formation of these narrow jets occurs during the nonlinear stage of the collapse, i.e. the perturbation amplitude is not small compared to either the disturbance wavelength or to the instant radius of the cavity, (ii) formation of the jets correlates with the onset of the second phase inversion, i.e. vorticity distribution along the bubble interface causes the interface to deflect such that the bubble amplitude starts to decrease, i.e. the bubble interface moves in the same direction as the narrow jets; (iii) the shape of the bubble just be-
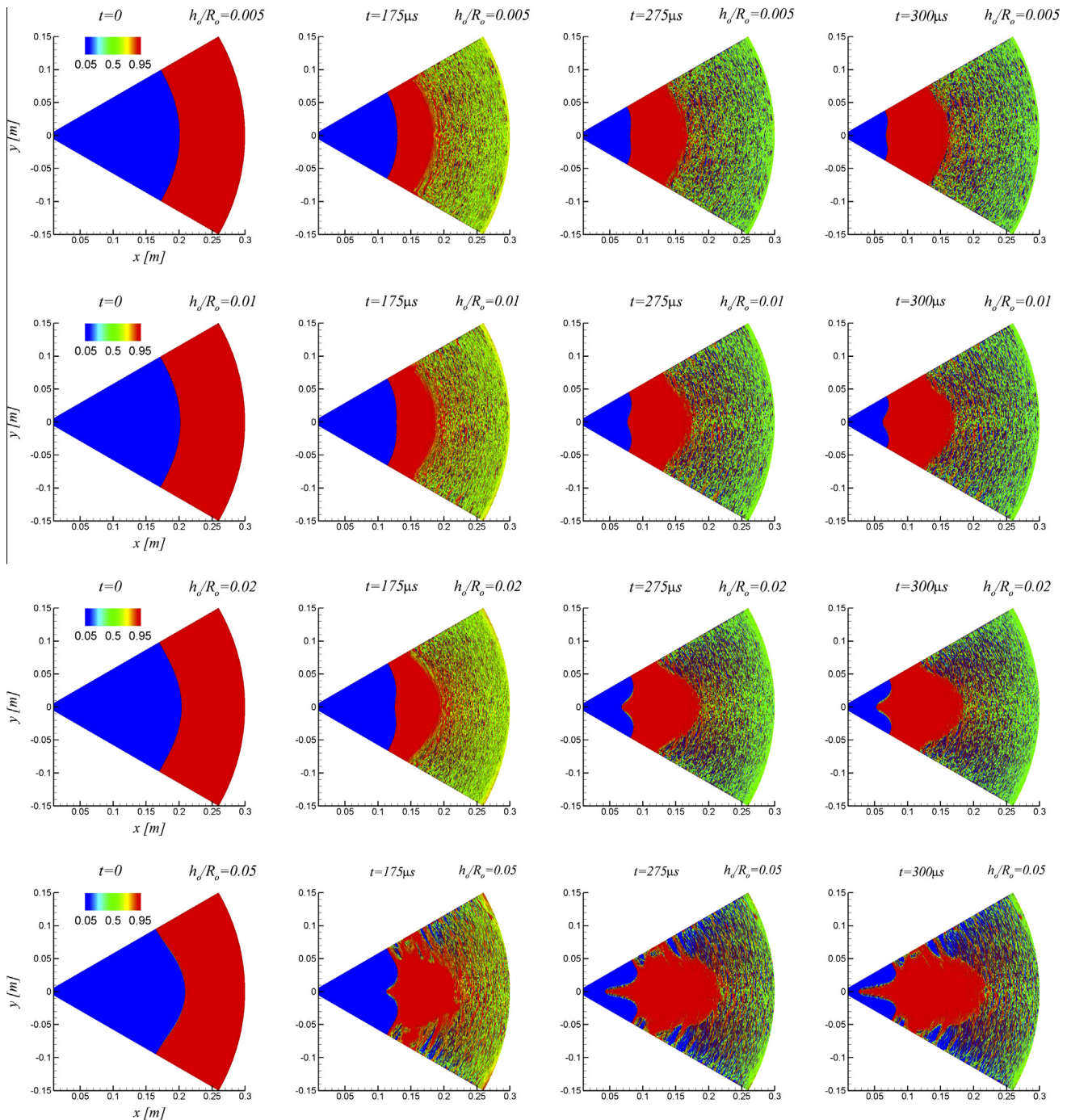

Fig. 14. Effect of initial perturbation amplitude shown by liquid phase fraction contours. Perturbation is at azimuthal mode $n = 6$, pulse pressure $P_{max} = 1.5$ GPa, pulse duration $T_{pulse} = 100$ μs. Each row of figure corresponds to a unique initial amplitude: $h_0 = 1$, 2, 4, and 10 mm; Cases N6A001, N6A002, N6A004, and N6A010 in Table 2.

fore the beginning of the jet formation does not appear to be as pointy as in experiments [37,38], but at the same time it definitely deviates from sinusoidal; (iv) the vorticities of opposite sign on each side of the bubble appear to interact at the head of the bubble and form the jets, (v) the interaction of vorticity sheets of opposite sign occurs only next to the bubbles, whereas at the head of the spike vorticity appears to be rather weak. As such, the formation of the narrow molten Pb jets depends on the azimuthal mode and amplitude of the perturbation and occurrence of the second phase inversion once the perturbation is in the nonlinear stage. The occurrence of the second phase inversion depends on the collapse trajectory characteristics and is discussed in Section 3.2.3. The conditions under which jets form in our simulations seem to agree with experimental observations in [37,38].

3.2.1. Effect of initial perturbation amplitude

The evolution of perturbations with various initial amplitudes is shown in Fig. 14 by liquid phase fraction contours. Rows in the figure correspond to the evolution of $n = 6$ perturbations with different initial amplitudes: cases N6A001, N6A002, N6A004 and N6A010 in Table 2. One can see that for the small-amplitude initial perturbation (first row) no significant nonlinear effects are observed and the spikes and bubbles remain nearly symmetric throughout the time period shown. As the amplitude increases, nonlinear effects begin to manifest themselves in the growing asymmetry between the spikes and bubbles. The spike appears to accelerate and becomes sharper, whereas the bubble appears to stagnate. For the current Atwood number of $A \approx -1$, the spikes are significantly sharper than those simulated for lower Atwood numbers. This has also been observed in numerical simulation of Tian et al. [16] as well as in experimental results of RM instability growth of solid and liquid metals in vacuum of Buttler et al. [24]. This is probably because in the case of such extreme density ratio, gas flow around the spike has a very little effect on the spike dynamics. Kelvin–Helmholtz instability, which is responsible for the formation of the mushroom like perturbation shape during the nonlinear stage for fluids with not to large density ratio, does not develop in the same manner in our case.

Fig. 14 also illustrates that the shape of the molten lead shell surrounding the gas cavity is affected by the initial imperfections of the interface. The distortion of the shell increases as the initial perturbation amplitude is increased. For the largest tested amplitude (row four), the thickness of the shell behind the bubble almost goes to zero.

Before proceeding to the plots of the evolution of spikes and bubbles, we would like to once more clarify the notation being used in all our plots. We follow extrema of the perturbation throughout the entire simulation, therefore our notation of 'spike' and 'bubble' corresponds to that usually used in the literature from the moment the phase inversion has occurred, as explained earlier in the validation section.

This is illustrated in Fig. 15 for the case N6A002 in Table 2. Part (a) shows a typical evolution of the spike (red broken line) and bubble (green dash-dot line) interface position along with the position of the initially unperturbed interface (black solid line). Part (b) of the figure shows the corresponding interface velocities. Time $t = 0$ corresponds to the moment when the pressure pulse hits the interface and the collapse begins. One can see that at $t = 0$, the red and green lines corresponding to the maximum and minimum of the initial perturbation are above and below the radial position of the initially unperturbed interface (black line), respectively, and the difference between those lines defines the amplitude of the initial perturbation h_0. The perturbation decreases in amplitude until around $t \approx 100$ μs (when phase inversion occurs) and then starts to grow in the opposite direction. From that moment our notation of 'spike' and 'bubble' matches that commonly used
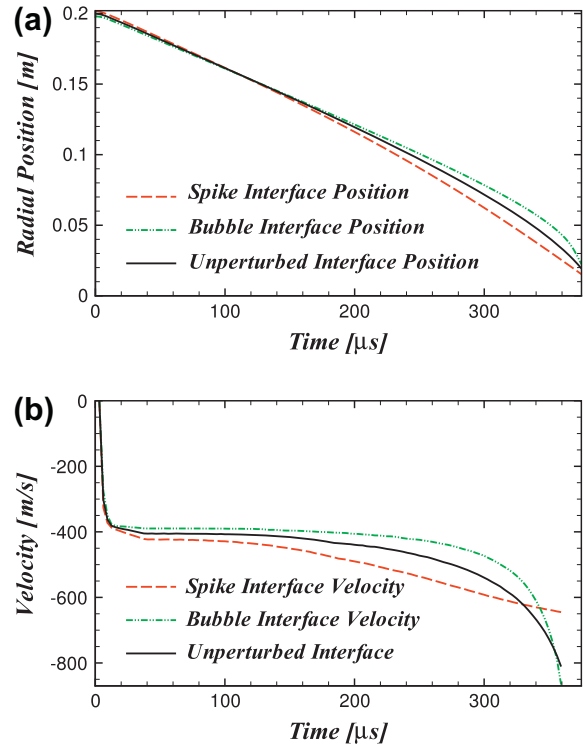

Fig. 15. (a) Typical position and (b) velocity of spike interface (red broken line), bubble interface (green dashed-dotted line), and initially unperturbed interface (black solid line) for case N6A002 in Table 2 with pulse pressure $P_{max} = 1.5$ GPa and pulse duration $T_{pulse} = 100$ μs. (For interpretation of the references to colour in this figure legend, the reader is referred to the web version of this article.)

in literature, i.e. a finger of light fluid poking into heavy fluid for a 'bubble', and that of heavy into light for a 'spike'.

At late stages of the collapse the difference between red and black lines as well as between green and black lines starts to decrease again eventually accompanied by another reversal, and in some cases by formation of the narrow molten lead jets. Fig. 15(b) shows the rapid acceleration of the interface resulting from its interaction with the pressure pulse. During early stages of the collapse, the velocities of the spikes, bubbles, and that of the unperturbed interface are nearly constant. Later the velocity of the unperturbed interface increases considerably due to the geometric convergence.

The effect of initial amplitude on the perturbation growth is shown in Fig. 16 for cases N6A001, N6A002, N6A004 and N6A010 in Table 2. The left column (parts a and b) and the right column (parts c and d) in Fig. 16 show the amplitude evolution of the spikes and bubbles, respectively. The top row shows the amplitude normalized by its initial value h_0, while the bottom row shows the amplitude normalized by the radius of the unperturbed gas cavity $R(t)$.

Examining the growth characteristics of the spike we can observe the following: (i) at early times growth of the spikes scales well with the initial perturbation amplitude for all amplitudes under consideration, (ii) after the phase inversion when the curves pass through zero for the first time, spike amplitude growth is faster for higher initial amplitudes, (iii) at large initial amplitudes the spike arrives at the center while it is still growing, so that no decrease of the spike amplitude is observed during the latest stages. For small initial amplitudes the spikes experience deceleration during late times, leading to a rapid decrease in spike amplitude. By comparing the growth characteristics of spikes and bubbles, it is apparent that the bubble amplitude does not scale as well with the initial perturbation amplitude, even early in the collapse. The
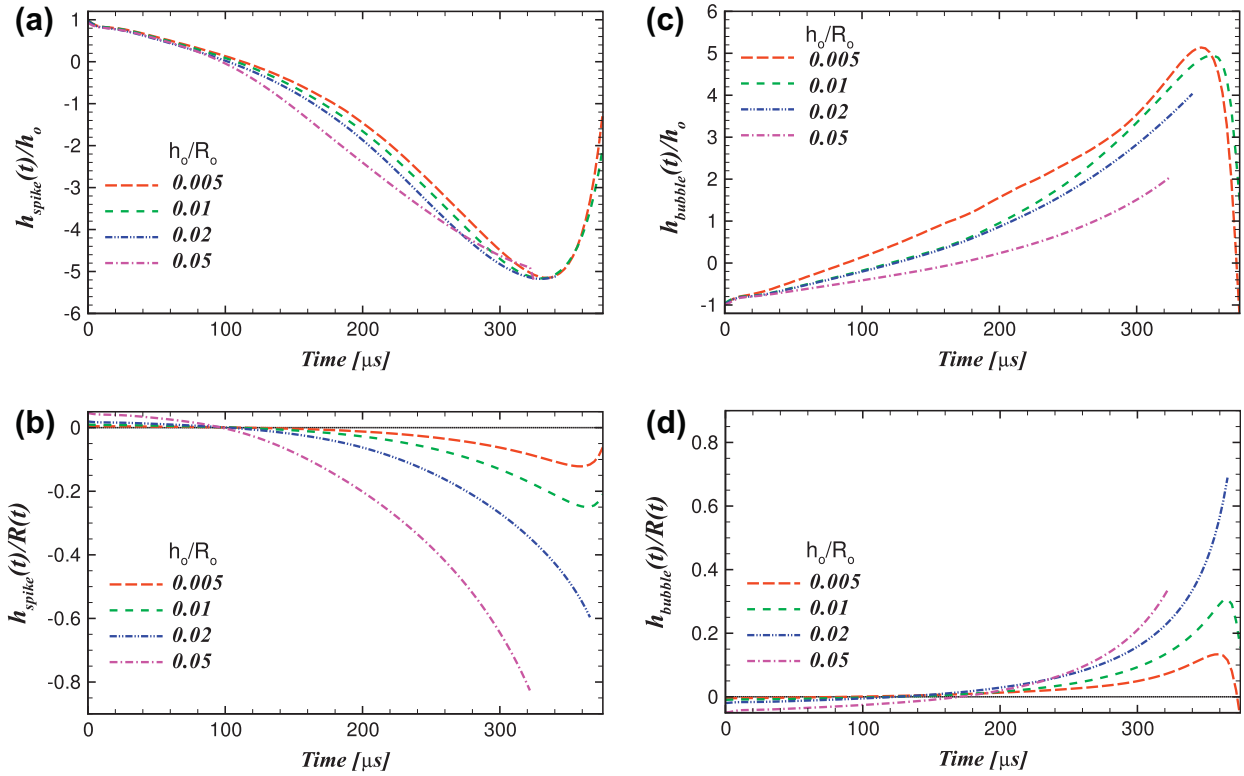
Fig. 16. Effect of initial amplitude on perturbation growth. Left and right columns correspond to spike and bubble evolution. (a) and (c) Evolution of normalized perturbation amplitude. (b) and (d) Evolution of ratio between perturbation amplitude and radius of unperturbed gas cavity. Azimuthal mode number $n = 6$ with pressure pulse $P_{max} = 1.5$ GPa and $T_{pulse} = 100$ μs.

bubble amplitude growth is significantly reduced for larger initial perturbations when compared to smaller ones. For the small-amplitude perturbations, a decrease in bubble amplitude can be seen at the latest stages. This decrease is related to formation of the rib-like jets and their rapid propagation toward the center of the cavity, as discussed earlier.

The effect of initial amplitude on the growth rates of spikes and bubbles is shown in Fig. 17. The left and right columns of the figure show the velocities of the spikes and bubbles (relative to the velocity of the unperturbed interface) corresponding to the data in Fig. 16. Dimensional velocities are plotted in the first row of the figure and the same velocities normalized by the corresponding velocity at $t = 40$ μs (immediately after the initial acceleration of the interface has been completed) are plotted in the second row. In Figs. 16(a) and (c) a negative velocity corresponds to the situation in which the perturbed interface (either spike or bubble) moves inwards faster than the initially unperturbed interface, whereas a positive velocity indicates that the perturbed interface moves inwards slower than the unperturbed interface (although it still moves inwards).

From the velocity plots one can see that after some finite initial time required to accelerate the interface from rest ($t \approx 40$ μs), the velocities of both spikes and bubbles approach a nearly constant value for a little while. This value is taken as the initial velocity that is used for scaling. Both spikes and bubbles undergo gradual acceleration until late times, when there is rapid deceleration, except for cases with large initial amplitudes in which the spikes reach the axis before this decelerate phase can occur. For all amplitudes under consideration, the bubble growth rate scales well with initial bubble velocity until the collapse is well underway. The spike growth rate also scales well, except for large amplitude perturbations, in which the growth rate saturates more quickly than the other cases.

3.2.2. Effect of azimuthal mode number

The behavior of spikes and bubbles is tested for various representative azimuthal mode numbers in the range $3 \leqslant n \leqslant 32$, with the results displayed in Fig. 18. The left columns (a)–(d) and the right columns (e)–(h) correspond to the evolution of spikes and bubbles, respectively. The first row of the figure (a) and (e) shows amplitude evolution of spikes and bubbles normalized by the initial perturbation amplitude h_0. The second row (b) and (f) shows the same data but with time scaled by the mode n. The third row of the figure (c) and (g) shows the perturbation amplitude normalized by the corresponding instantaneous cavity radius $R(t)$ for the initially unperturbed interface. Finally, the fourth row (f) and (g) shows the same data normalized by the corresponding instantaneous perturbation wave length $\lambda(t)$.

From the plots in the first two rows of Fig. 18 the following can be observed: (i) for the setup and parameters under consideration the perturbation evolution at low azimuthal numbers ($n = 3, 4$) differs from that at higher azimuthal mode numbers. In particular, the decrease in the perturbation amplitude (and in most cases a second phase inversion) observed at higher azimuthal modes at the latest stages of the collapse does not occur at low azimuthal mode numbers; (ii) at higher azimuthal modes ($n = 24, 32$) the maximum amplitude attained by spikes is significantly higher than that of bubbles; (iii) the first phase inversion time roughly scales with the azimuthal mode number; (iv) the second phase inversion, often accompanied by the formation of the narrow jets (ribs) at the head of each bubble is clearly seen in parts (b) and (f) of the figure. However, in the case of large azimuthal mode, the cavity collapses before the second phase inversion is completed, as can be seen from the $n = 32$ curves.

Results presented in the third and fourth rows of Fig. 18 emphasize convergence and nonlinear effects, respectively. One can see that convergence effects, expressed by ratio $h(t)/R(t)$ (c and g), be-
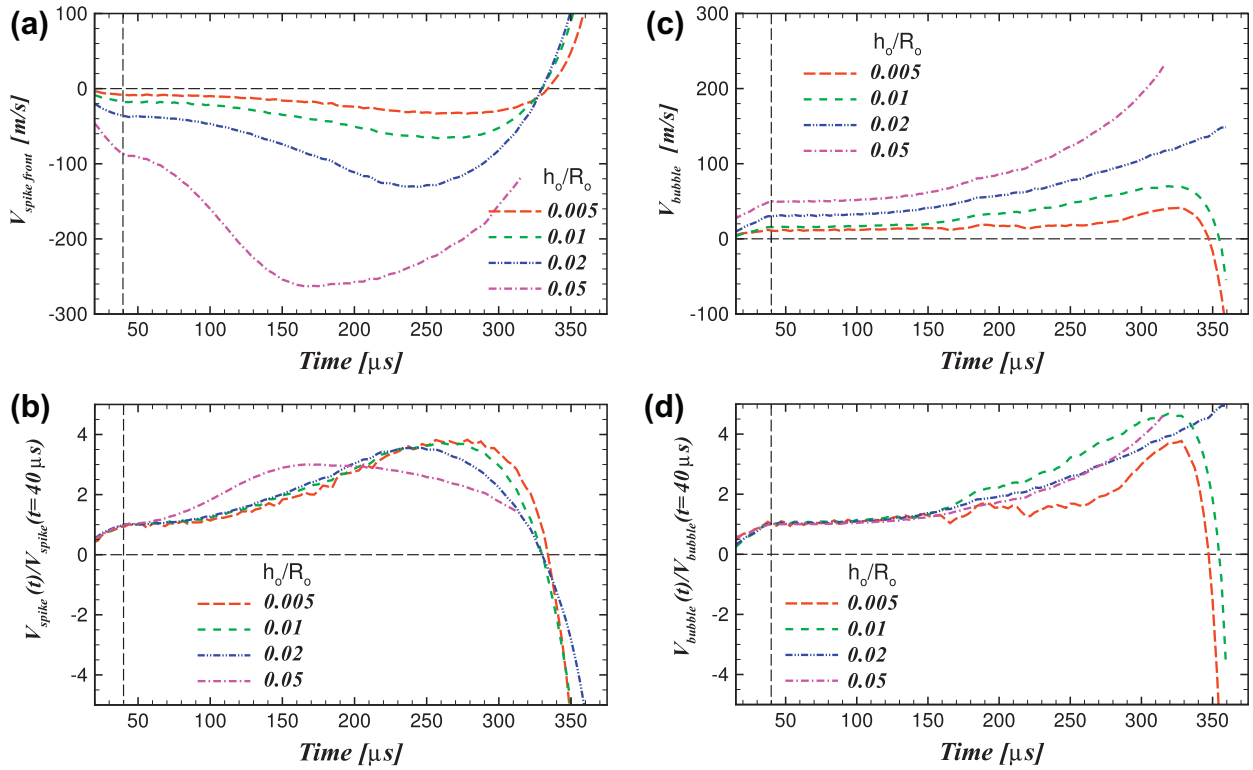
Fig. 17. Effect of initial amplitude on perturbation growth rate. Left and right columns correspond to spike and bubble evolution, respectively. (a) and (c) Perturbation growth rate. (b) and (d) Perturbation growth rate normalized by its initial growth rate at $t = 40$ μs. Azimuthal mode number $n = 6$ with pulse pressure $P_{max} = 1.5$ GPa and pulse length $T_{pulse} = 100$ μs.

come significant for all azimuthal modes at some point during the collapse. For the current set of simulations with the same initial ratio h_0/R_0 for all modes, the ratio $h(t)/R(t)$ grows faster for larger azimuthal mode numbers. The lower azimuthal modes are also influenced by convergence during the entire collapse, as they have high values of $\lambda(t)/R(t)$, i.e. they 'see' the curvature of the interface at all times. With respect to the nonlinear effects (d and h), one can see that a significant degree of nonlinearity is reached by all perturbations during the collapse. Perturbations with higher azimuthal modes undergo higher initial growth rates and consequently experience nonlinear effects earlier in the collapse, thereby attaining a higher degree of nonlinearity. This explains the growing disparity between spike and bubble amplitudes as the azimuthal mode number increases, as seen in the first and second rows of the figure.

For the sake of completeness, the width of the mixing layer expressed as a difference between radial position of the spike and bubble interfaces (difference between broken red and dash-dot green lines in Fig. 15) is shown in Fig. 19 for all azimuthal modes. The plotted mixing layer width ($R_{spike} - R_{bubble}$) is normalized by $2h_0$ so that its initial value is one. At low azimuthal modes ($n = 3$, 4) the width of the mixing layer gradually decreases for a significant portion of the collapse (as the first phase inversion takes place), followed by some increase before its growth slows down again as the interface approaches $r = 0$. As the azimuthal mode number increases, the mixing layer width undergoes more or less monotonic growth for some time after the first phase inversion. Then it starts to decrease and for azimuthal modes $n \geqslant 6$ crosses zero again. For the current set of simulations, the second reversal of the mixing layer width sign corresponds to the situation when narrow jets (ribs), which appear at the head of the bubble, reach the origin before arrival of the original spike (see Fig. 13).

3.2.3. Comparison with existing models for small-amplitude perturbations

In this section we compare our results with the Mikaelian theoretical model [18] for small-amplitude disturbances in cylindrical geometry. The evolution of small-amplitude perturbations in cylindrical geometry for an arbitrary collapse history is governed by the following equation (Eq. 1b in [18]):

$$\frac{d^2h}{dt^2} + 2\frac{\dot{R}}{R}\frac{dh}{dt} - (nA - 1)\frac{\ddot{R}}{R}h = 0, \tag{8}$$

where h is the perturbation amplitude, R, $\dot{R}$ and $\ddot{R}$ are position, velocity and acceleration history of the unperturbed interface, n is the mode number of the perturbation and A is the Atwood number.[3] Assuming the interface moves with constant velocity after the shock (pure RM instability), the solution of Eq. (8) simplifies to the following expression (Eq. 3b in [18]):

$$h(t) = h(0)[1 + (nA - 1)(1 - R_0/R)]. \tag{9}$$

Using the collapse trajectory from our simulation of the unperturbed interface, we calculated perturbation evolution with both methods: solving the Eq. (8) and using Eq. (9) that assumes a constant interface velocity. The following boundary conditions have been used to solve Eq. (8),

$$h(t = 0) = h_0, \quad \dot{h}(t = 0) = \dot{h}_{cylindrical}. \tag{10}$$

The initial perturbation growth rate was calculated by the following equation [18],

---

[3] Atwood number in Eq. (8) is defined according to Mikaelian [18] which is of an opposite sign to our definition, i.e. our $A = -1$ corresponds to $A = 1$ in [18].
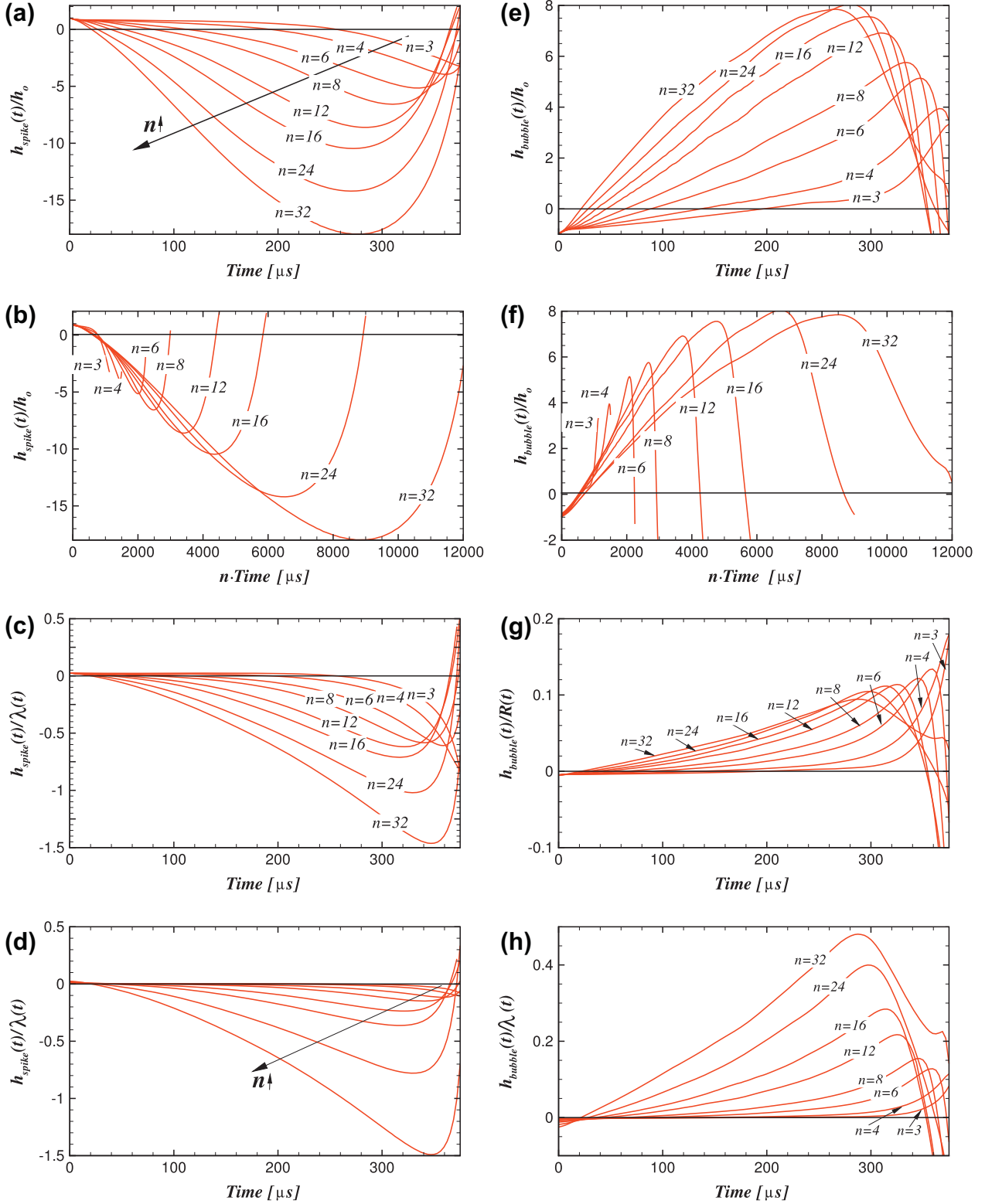
Fig. 18. Effect of azimuthal mode number *n* on perturbation growth. Left and right columns correspond to spike and bubble evolution, respectively. (a) and (e) Perturbation amplitude normalized by its initial amplitude h_0. (b) and (f) Same but with time scaled by mode *n*. (c) and (g) Perturbation amplitude normalized by radial position of unperturbed interface. (d) and (h) Perturbation amplitude normalized by perturbation wavelength. Pressure pulse with $P_{max} = 1.5$ GPa and $T_{pulse} = 100$ μs.

$$\dot{h}_{\text{cylindrical}} = (nA - 1)\frac{h_0}{R_0}V_{\text{interface}}, \tag{11}$$

where R_o and $V_{\text{interface}}$ are the initial radial position and velocity of unperturbed interface, respectively.

For completeness, the initial perturbation growth rate for a planar case and small- amplitude perturbation is given by [1] as:

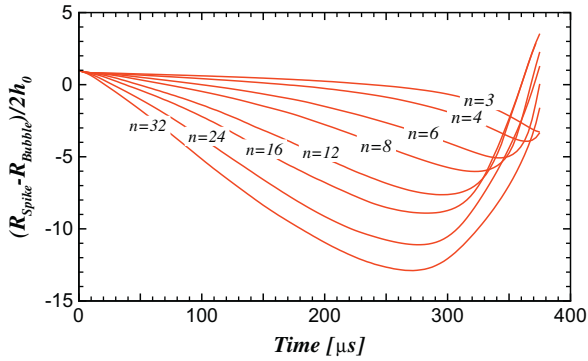$$\dot{h}_{\text{planar}} = h_0 k A V_{\text{interface}}, \tag{12}$$

Fig. 19. Effect of azimuthal mode number n on evolution of normalized mixing layer thickness defined as $(R_{\text{spike}} - R_{\text{bubble}})/2h_0$. Pressure pulse with $P_{\max} = 1.5$ GPa and $T_{\text{pulse}} = 100$ μs.

where as usual, h_0 denotes the initial perturbation amplitude, A is the Atwood number, $k = 2\pi/\lambda = n/R_0$ is the wave number, n is the azimuthal mode, and $V_{\text{interface}}$ is the initial velocity of the undisturbed interface (see Eq. (4)).

Fig. 20 shows the collapse history used to solve Eqs. (8) and (9); the trajectory of the interface, its velocity and acceleration are shown, respectively, by the red solid line, blue broken line and green dash-dotted line. We can see that after the initial rapid acceleration of the interface, its velocity remains nearly constant until geometric convergence becomes important and the interface undergoes acceleration through the rest of the collapse. We allowed gas to escape from the domain so the gas pressure never gets high enough to cause deceleration of the shell.

Comparison between our numerical results and the Mikaelian theoretical model [18] is shown in Fig. 21 for perturbations with different azimuthal modes. Evolution of the spikes and bubbles obtained in our simulations is plotted by a red solid line with filled symbols and a green solid line with hollow symbols, respectively. The black solid and broken lines correspond to the theoretical models [18] given by Eqs. (8) and (9), respectively. When comparing the theoretical models one can see that they are almost identical for the initial 150–250 μs but after that begin to diverge. When a constant velocity of the interface is assumed (black broken line) the perturbation grows monotonically throughout the collapse after the first phase inversion. However, when the exact collapse history is used (black solid line), the perturbation growth exhibits an oscillatory behavior with additional phase inversions that becomes more pronounced as the collapse proceeds and also varies

with azimuthal mode number. The oscillatory behavior predicted by Eq. (8) is attributed to the inward acceleration of the interface that becomes more prominent during the late stages of the collapse. One can see that the third term in Eq. (8), $\left[(nA - 1)\frac{\ddot{R}}{R}\eta \right]$, increases with acceleration and azimuthal mode number. This explains why the disparity between the two models (black solid and broken lines in Fig. 21) manifests itself earlier at higher azimuthal modes, despite having the same acceleration history.

The excellent agreement between our numerical results and the theoretical model given by Eq. (8) can be seen by comparing the red and green lines with symbols with the black solid line in Fig. 21. At low azimuthal modes (a and b) the growth rates predicted by the models are somewhat higher than those obtained in simulations, but the behavior is reproduced correctly. For the perturbations with azimuthal mode numbers within the range $6 \leqslant n \leqslant 16$ (c, d, e and f of the figure) the agreement between numerical and theoretical results is remarkable. The second phase inversion, which is accompanied by the formation of narrow jets from the heads of bubbles in our simulations, is accurately captured by the theoretical model. At high azimuthal mode numbers (g and h) the oscillatory behavior predicted by the model is of a shorter period compared to our numerical results but again the overall behavior is captured very well. For high azimuthal mode number perturbations, the nonlinear effects become prominent quite early in the collapse (see Fig. 18), resulting in disparity between spike and bubble evolution. Therefore, it is not unexpected that our results for high azimuthal numbers deviate from those predicted by the model which is valid for the small-amplitude perturbations. Nevertheless, the amplitude predicted by this model agrees well with that for spikes obtained in simulation, whereas the amplitude of the bubble is overestimated.

There are two more points we would like to add regarding the Mikaelian theoretical model (Eq. (8)). The first one is that the results predicted by this model are robust with regard to small oscillations in the acceleration history. We used both smoothed and randomly oscillating (direct from the numeric results) acceleration history for the solution of Eq. (8) and the results were basically the same. Insensitivity of the solution to small oscillations in the acceleration history was also reported by Mikaelian [39]. The second point is that the somewhat oscillatory behavior observed at late stages of the collapse is essentially the same as the linear oscillations known to occur during gravity-driven collapse of a gas bubble. An illustration of such oscillations can be found in recent work [38], for example.

Finally, in Fig. 22 we present initial perturbation growth rates for the different azimuthal mode numbers taken at $t \approx 40$ μs, after
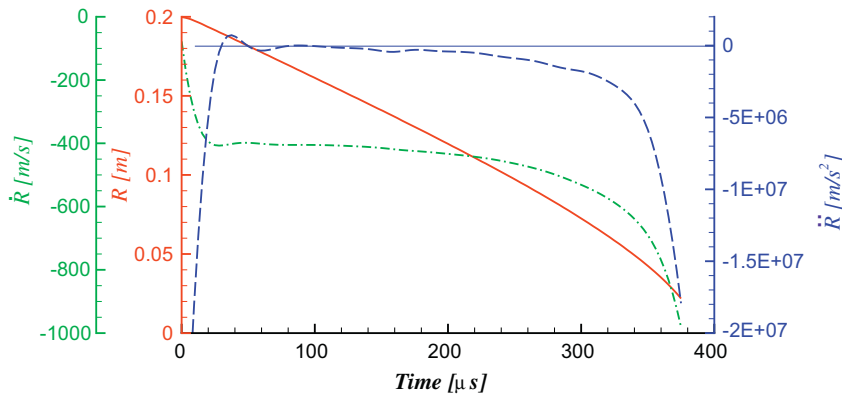

Fig. 20. Collapse history of unperturbed gas cavity used for calculation of linear perturbation growth according to Mikaelian [18]. Interface trajectory R, interface velocity $\dot{R}$ and interface acceleration $\ddot{R}$ are shown correspondingly by the solid red line, dash-dot green line and broken blue line. Collapse history is for pressure pulse with $P_{\max} = 1.5$ GPa and $T_{\text{pulse}} = 100$ μs. (For interpretation of the references to colour in this figure legend, the reader is referred to the web version of this article.)
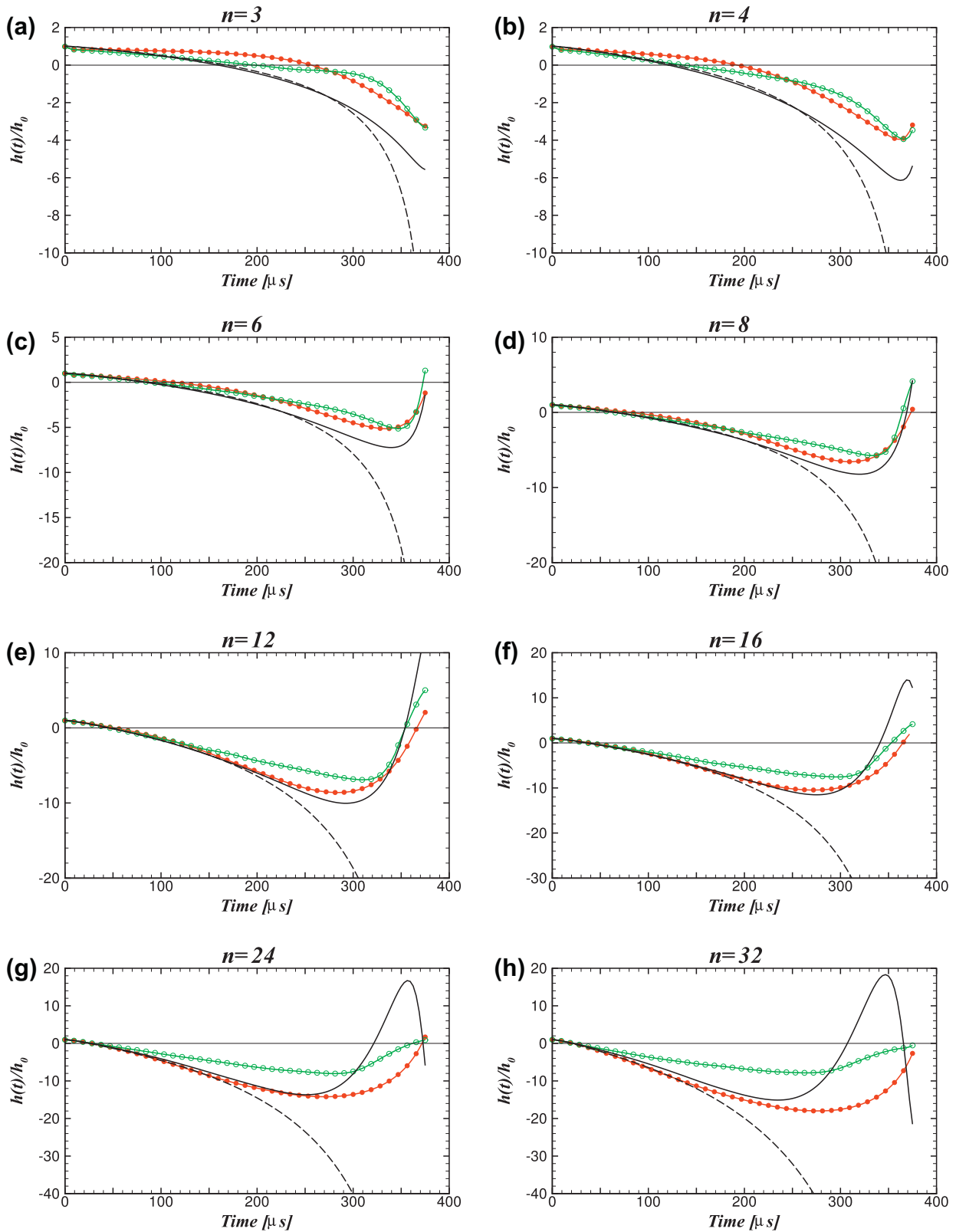
Fig. 21. Comparison between our numerical results and small-amplitude theoretical model of Mikaelian [18] for perturbation growth normalized by its initial amplitude h_0 at different azimuthal numbers *n*. Spike and bubble amplitudes are shown by red lines with filled symbols and green lines with hollow symbols, respectively. Theoretical models given by Eqs. (8) and (9) are shown by black solid and broken lines, respectively. (For interpretation of the references to colour in this figure legend, the reader is referred to the web version of this article.)

the initial acceleration of the interface has been completed. Our results for the growth rates of spikes and bubbles are shown by red triangles and green circles, respectively. Data obtained from the two linear models, for planar geometry by Richtmyer [1] (Eq. (12)) and for cylindrical geometry by Mikaelian [18] (Eq. (11)), are shown by solid and broken lines, respectively. The growth rates
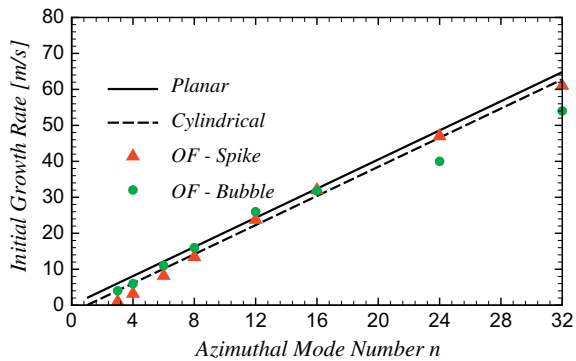
Fig. 22. Effect of azimuthal mode number on perturbation early growth rate. Red triangles and green circles correspond to initial growth rates of spikes and bubbles, respectively. Solid and broken lines correspond to planar model of Richtmyer [1] (Eq. (12)) and cylindrical model of Mikaelian [18] (Eq. (11)), respectively. Pressure pulse with $P_{max} = 1.5$ GPa and $T_{pulse} = 100$ μs. (For interpretation of the references to colour in this figure legend, the reader is referred to the web version of this article.)

presented in Fig. 22 show encouraging agreement with the linear models for the range of perturbations being considered. However, it is apparent that the growth rates change for the higher azimuthal modes ($n > 16$ in our data set). This is probably because there are more pronounced nonlinear effects at those modes: in all our simulations the parameter h_o/R_o has been kept constant and therefore, the parameter h_o/λ_o increases with the azimuthal mode number of the perturbation.

To summarize, the *initial* growth rates can be predicted quite well by both planar and cylindrical models, but if growth rates during the entire evolution are of interest, then a theoretical model that properly accounts for the effects of cylindrical geometry and a prescibed collapse history should be used.

4. Summary

In this work, the development of the Richtmyer–Meshkov instability was studied for the case of a cylindrical gas bubble compressed by an imploding Pb lead shell. The main contribution of this work is to explore the RM instability in the extreme regime of Atwood number $A = -1$ with a liquid as one of the working fluids. Our motivation is to estimate the minimum smoothness required to achieve efficient compression of the gas cavity. Simulations have been performed using the OpenFOAM software for a set of parameters relevant to the prototype compression system under development at General Fusion Inc. as a driver for magnetized target fusion. The main results and conclusions are summarized below:

- In the regime of Atwood number $A = -1$, there is a disparity between the growth rates of spikes and bubbles; spikes undergo acceleration while bubbles move at nearly constant velocity. This disparity in growth rates becomes more prominent as the amplitude of the initial perturbation is increased.
- The shape of the spikes obtained for the current set of parameters is different from that usually observed in the regime of moderate Atwood numbers. The spikes retain a sharp pointy structure and do not develop into the typical mushroom shape. This is an agreement with existing numerical [16] and experimental [24] results. This difference in the shape is likely to be related to the differences in the development of the Kelvin–Helmholtz instability at extreme and moderate Atwood numbers, as the Kelvin–Helmholtz instability is the main mechanism behind the development of the mushroom shape at moderate Atwood numbers.

- During the late stages of the collapse the perturbation amplitude decreases again, resulting in a second phase-inversion for higher azimuthal modes. This kind of oscillatory behavior is attributed to the inward acceleration of the interface that increases as the cavity radius decreases.
- The formation of narrow molten lead jets propagating inwards and originating from the head of the bubbles has been observed later in the collapse for modes $n > 4$. These jets are formed during the nonlinear stage of collapse and correlate with the onset of the second phase inversion. Our results indicate that they are caused by the interaction of vorticity sheets of opposite sign at the head of the bubble. To the best of our knowledge, these jets have not been observed at a gas–gas interface with moderate Atwood number.
- A comparison of our numerical results with the recent theoretical model of Mikaelian [18] for small-amplitude perturbations shows good agreement. Further testing of this model to study the range of its applicability and limitations is highly desirable.
- To maintain sufficient compression efficiency, low-mode interface perturbations are not likely to be detrimental. However, high-mode perturbations are problematic and must be kept to a minimum.
- The Open-source CFD code OpenFOAM and the current numerical setup seems to capture relevant physics and produce valuable results.

The numerical setup used in the present work can be further extended to include more physics. (i) The isothermal assumption could be eliminated to better understand energy losses during the pulse propagation through the molten lead, which is important for stronger pressure pulses and shocked up fronts. (ii) A more sophisticated cavitation model could be added to better model the formation of the molten Pb shell resulting from the interaction between the pressure pulse and the liquid–gas interface. (iii) A more sophisticated equation of state for the gas could include temperature and magnetic stress effects. The correct dynamics of the gas (plasma) late in the collapse is crucial as it is responsible for the deceleration of the interface and this deceleration will affect perturbation evolution. (iv) Effects of the magnetic field on the dynamics of the molten lead could be added.

Some of this work is currently in progress. In addition to incorporating more physics into simulation, we intend to study effects of the pressure pulse shape and fluid rotation.

Appendix A. 'compressibleInterFoam'

The solver **'compressibleInterFoam'** is based on the solver **'interFoam'** [40] and extends it to account for fluid compressibility effects. A detailed description and implementation of the **interFoam** solver as well as its evaluation can be found in a recent work by Deshpande et al. [41]. Additional details of implementation of the Volume-of-fluid (VOF) method in OpenFOAM can be also found in the Ph.D. Thesis of Rushe [42]. The governing equations solved in **'compressibleInterFoam'** are given below:

Mass continuity Equation:

$$\frac{\partial \rho}{\partial t} + \nabla \cdot (\rho \mathbf{U}) = 0. \tag{A1}$$

Continuity equation for each of the phases:

$$\frac{\partial \rho \alpha_i}{\partial t} + \nabla \cdot (\rho \alpha_i \mathbf{U}_i) = 0, \tag{A2}$$

where the subscript i denotes the phase and α is the phase fraction. (The exact form of the phase conservation equation solved in **'compressibleInterFoam'** is derived and discussed later.)

Momentum equation:

$$\frac{\partial \rho \mathbf{U}}{\partial t} + \triangledown \cdot (\rho \mathbf{U}\mathbf{U}) = -\triangledown \left(P + \frac{2}{3}\mu \triangledown \cdot \mathbf{U}\right)$$
$$+ [\triangledown \cdot (\mu \triangledown \mathbf{U}) + \triangledown \mathbf{U} \cdot \triangledown \mu] + \rho \mathbf{g}$$
$$+ \int_{\Gamma} \sigma \kappa \delta(\mathbf{x} - \mathbf{x}_s)\mathbf{n}\,d\Gamma(\mathbf{x}_s), \tag{A3}$$

where Γ is the gas–liquid interface, $\delta(\mathbf{x} - \mathbf{x}_s)$ is the three-dimensional Dirac delta function. The force of surface tension is calculated using the continuum surface force (CSF) model of Brackbill et al. [43]. The integral form of the surface tension term is given by:

$$\int_{\Gamma \bigcap \Omega_i} \sigma \kappa \mathbf{n}\,d\Gamma(\mathbf{x}_s) = \int_{\Omega_i} \sigma \kappa \triangledown \alpha_1\,dV, \tag{A4}$$

where σ is the surface tension, κ is the curvature of the free surface and α_1 is the phase fraction of phase 1. Curvature of the free surface is calculated from the phase fraction α_1 as $\kappa = -\triangledown \cdot \left(\frac{\triangledown \alpha_1}{|\triangledown \alpha_1|}\right)$.

Equation of state: In the current study OpenFOAM version 1.7.1 was used. In this version both fluids are assumed to be isothermal and a barotropic equation of state is implemented as:

$$\rho_i = \rho_{oi} + \psi_i P, \tag{A5}$$

where the subscript i denotes the phase and ψ is the compressibility $\psi = 1/c^2$ with c being the speed of sound. For a gas (compressible phase) the nominal density ρ_o is set to zero. This results in an ideal gas equation of state for an isothermal fluid. For a liquid (low compressibility phase) ρ_o is set to the nominal density of the liquid under normal conditions. Both fluids are treated as a single fluid "mixture" whose properties vary in space according to the volume fraction of each phase:

$$\rho = \alpha_1 \rho_1 + \alpha_2 \rho_2, \quad \mu = \alpha_1 \mu_1 + \alpha_2 \mu_2, \quad where\ \alpha_1 + \alpha_2 = 1. \tag{A6}$$

The same is valid for velocity $\mathbf{U}$ in Eqs. (A1) and (A3), i.e. $\mathbf{U} = \alpha_1 \mathbf{U}_1 + \alpha_2 \mathbf{U}_2$.

Derivation of phase fraction continuity equation: The discretization of the convective term in Eq. (A2) is crucial and low-order schemes are known to smear the interface [26]. In OpenFOAM this equation is modified in such a way that it includes an additional 'compression' term that helps to prevent smearing of the interface. We first show the derivation of the 'compression' term for the incompressible flow, as it is implemented in **'interFoam'** by Rushe [42], and then extend derivation to the compressible case.

For incompressible fluid the equation of phase continuity is given by:

$$\frac{\partial \alpha_i}{\partial t} + \triangledown \cdot (\alpha_i \mathbf{U}_i) = 0, \tag{A7}$$

where the subscript i denotes the phase and α is the phase fraction. Eq. (A7) can be re-arranged [44] as:

$$\frac{\partial \alpha_1}{\partial t} + \triangledown \cdot (\alpha_1 \mathbf{U}) + \triangledown \cdot (\alpha_1(1 - \alpha_1)\mathbf{U_r}) = 0, \tag{A8}$$

where volumetric velocity $\mathbf{U}$ is defined as $\mathbf{U} = \alpha_1 \mathbf{U}_1 + \alpha_2 \mathbf{U}_2$ and a relative ('compression') velocity $\mathbf{U_r}$ is defined as $\mathbf{U_r} = \mathbf{U}_1 - \mathbf{U}_2$. The third term in Eq. (A8) is an artificial compression term which is only active in the thin interface region because of the multiplication term $\alpha_1(1 - \alpha_1)$. As such, it does not affect the solution significantly outside this region.

For compressible flow, Eq. (A2) can be re-written as:

$$\frac{\partial \alpha_i}{\partial t} + \triangledown \cdot (\alpha_i \mathbf{U}_i) = -\frac{\alpha_i}{\rho_i}\frac{D\rho_i}{Dt}. \tag{A9}$$

We can rewrite the relation between density and pressure given by Eq. (A5) as:

$$\frac{D\rho_i}{Dt} = \psi_i \frac{DP}{Dt}, \tag{A10}$$

which can be inserted into Eq. (A9) to get:

$$\frac{\partial \alpha_i}{\partial t} + \triangledown \cdot (\alpha_i \mathbf{U}_i) = -\frac{\alpha_i \psi_i}{\rho_i} \cdot \frac{DP}{Dt}. \tag{A11}$$

By adding equations for each phase in Eq. (A11), the divergence of the volumetric velocity $\mathbf{U}$ can be calculated as

$$\triangledown \cdot \mathbf{U} = -\left(\frac{\alpha_1 \psi_1}{\rho_1} + \frac{\alpha_2 \psi_2}{\rho_2}\right)\frac{DP}{Dt}. \tag{A12}$$

The L.H.S. of Eq. (A11) is the same as that of Eq. (A7) and, therefore, can be re-arranged as in Eq. (A8). We can add and subtract the term $\alpha_1 \triangledown \cdot \mathbf{U}$ to the R.H.S. of Eq. (A11) (which is treated as a source term). Then the equation for phase continuity of an compressible flow can be written as:

$$\frac{\partial \alpha_1}{\partial t} + \triangledown \cdot (\alpha_1 \mathbf{U}) + \triangledown \cdot (\alpha_1(1 - \alpha_1)\mathbf{U_r}) = \alpha_1(1 - \alpha_1)dgdt + \alpha_1 \triangledown \cdot \mathbf{U}, \tag{A13}$$

$$where\quad dgdt = (\psi_2/\rho_2 - \psi_1/\rho_1)\frac{DP}{Dt}.$$

The L.H.S. of Eq. (A13) is identical to the L.H.S of Eq. (A8) and the details of the numerical implementation can be found in [41,42]. The R.H.S. of Eq. (A13) is treated as the source term. Implementation of the source term in OpenFOAM (which can be implicit or explicit) is explained in the Programmer's Guide [45].

The overall numerical procedure for solving the governing equations is similar to that used in the **interFoam** solver, detailed description of which can be found in Rushe [42] and Deshpande et al. [41]. An additional outer correction loop is required in **'compressibleInterFoam'** to accommodate compressibility effects.

References

[1] Richtmyer RD. Taylor instability in shock acceleration of compressible fluids. Commun Pure Appl Math 1960;13:297–319.

[2] Meshkov EE. Instability of the interface of two gases accelerated by a shock wave. Fluid Dyn 1969;4(5):101–4.

[3] Laberge M. Experimental results for an acoustic driver for MTF. J Fusion Energy 2009;28:179–82.

[4] General Fusion Inc., www.generalfusion.com.

[5] Dimonte G, Ramaprabhu P. Simulations and model of the nonlinear Richtmyer–Meshkov instability. Phys Fluids 2010;22:014104.

[6] Brouillette M. The Richtmyer–Meshkov instability. Annu Rev Fluid Mech 2002;34:445–68.

[7] Zabusky NJ. Vortex paradigm for accelerated inhomogeneous flows: visiometrics for the Rayleigh–Taylor and Richtmyer–Meshkov environments. Annu Rev Fluid Mech 1999;31:495–536.

[8] Zhang Q, Graham MJ. A numerical study of Richtmyer–Meshkov instability driven by cylindrical shocks. Phys Fluids 1998;10:974–92.

[9] Yang Y, Zhang Q, Sharp DH. Small amplitude theory of Richtmyer–Meshkov instability. Phys Fluids 1994;6:1856–73.

[10] Holmes RL, Dimonte G, Fryxell B, Gittings ML, Grove JW, Schneider M, et al. Simulation and theory. J Fluid Mech 1999;389:55–79.

[11] Latini M, Schilling O, Don WS. High-resolution simulations and modeling of Reshocked single-mode Richtmyer–Meshkov instability: comparison to experimental data and to amplitude growth model predictions. Phys Fluids 2007;19:024104.

[12] Nishihara K, Wouchuk JG, Matsuoka C, Ishizaki R, Zhakhovsky VV. Richtmyer–Meshkov instability: theory of linear and nonlinear evolution. Phil Trans R Soc A 2010;368:1769–807.

[13] Thornber B, Drikakis D, Youngs DL, Williams RJR. The influence of initial conditions on turbulent mixing due to Richtmyer–Meshkov instability. J Fluid Mech 2010;654:99–139.

[14] Cohen RH, Dannevik WP, Dimits AM, Eliason DE, Mirin AA, Zhou Y. Three-dimensional simulation of a Richtmyer–Meshkov instability with a two-scale initial perturbation. Phys Fluids 2002;14:3692–709.

[15] Fincke JR, Lanier NE, Batha SH, Hueckstaedt RM, Magelssen GR, Rothman SD, et al. Postponement of saturation of the Richtmyer–Meshkov instability in a convergent geometry. Phys Rev Lett 2004;93(11):115003.

[16] Tian B, Fu D, Ma Y. Numerical investigation of Richtmyer–Meshkov instability driven by cylindrical shocks. Acta Mech Sinica 2006;22:9–16.

[17] Krechetnikov R. Rayleigh–Taylor and Richtmyer–Meshkov instabilities of flat and curved interfaces. J Fluid Mech 2009. 625-387.

[18] Mikaelian KO. Rayleigh–Taylor and Richtmyer–Meshkov instabilities and mixing in stratified cylindrical shells. Phys Fluids 2005;17:094105.

[19] Lombardini M, Pullin DI. Small-amplitude perturbations in the three-dimensional cylindrical Richtmyer–Meshkov instability. Phys Fluids 2009;21:114103.

[20] Schilling O, Latini M, Don WS. Physics of Reshock and mixing in single-mode Richtmyer–Meshkov instability. Phys Rev E 2007;76:026319.

[21] Schilling O, Latini M. High-order WENO simulations of three-dimensional reshocked Richtmyer–Meshkov instability to late times: dynamics, dependence on initial conditions, and comparisons to experimental data. Acta Mech Sci 2010;30B:595–620.

[22] Móran-López JT, Schilling O. Multicomponent Reynolds-averaged Navier–Stokes simulations of reshocked Richtmyer–Meshkov instability-induced mixing. High Energy Phys 2013;9:112–21.

[23] Ward GM, Pullin DI. A study of planar Richtmyer–Meshkov instability in fluids with Mie-Gruneisen equations of state. Phys Fluids 2011;23:076101.

[24] Buttler WT, Oro DM, Preston DL, Mikaelian KO, Cherne FJ, Hixson RS, et al. Unstable Richtmyer–Meshkov growth of solid and liquid metals in vacuum. J Fluid Mech 2012;703:60–84.

[25] OpenCFD Ltd. at ESI group, www.openfoam.com.

[26] Ferziger JH, Peric M. Computational methods for fluid dynamics. 2nd ed. Springer-Verlag; 1997.

[27] Issa RI. Computational methods for fluid dynamics. J Comput Phys 1986;62:40–65.

[28] Tait PG. Report on some of the physical properties of fresh water and sea water. Rept Sci Results Voy, HMS Challenger, Phys Chem 1888;2:1–76.

[29] LS-DYNA – Livermore Software Technology Corporation, http://www.lstc.com/products/ls-dyna.

[30] Handbook on Lead-bismuth Eutetic Alloy and Lead Properties, Materials Compatibility, Thermal-hydraulics and Technologies, OECD Nuclear Energy Agency. Nuclear Science Committee, London, UK; 2007.

[31] Thompson PA. Compressible fluid dynamics. Maple Press Company; 1984.

[32] Landau LD, Lifshitz EM. Fluid mechanics. 2nd ed. Pergamon Press; 1987.

[33] Courant R, Friedrichs KO. Supersonic flow and shock waves. Springer-Verlag; 1976.

[34] Kedrinskii VK. Hydrodynamics of explosion. Springer-Verlag; 2005.

[35] Cole RH. Underwater explosions. New York: Dover; 1965.

[36] Suponitsky V, Barsky S, Froese A. On the collapse of a gas cavity by an imploding molten lead shell and Richtmyer–Meshkov instability. In: Proceedings of the 20th annual conference of the CFD society of Canada, Canmore, Alberta, Canada, May 9–11; 2012.

[37] Enriquez OR, Peters IR, Gekle S, Schmidt LE, Versluis M, et al. Collapse of nonaxisymmetric cavities. Phys Fluids 2010;22:091104.

[38] Enriquez OR, Peters IR, Gekle S, Schmidt LE, Lohse D, van der Meer D. Collapse and pinch-off of a non-axisymmetric impact-created air cavity in water. J Fluid Mech 2012;701:40–58.

[39] Mikaelian KO. Analytic approach to nonlinear hydrodynamic instabilities driven by time-dependent accelerations. Phys Rev E 2010;91:016325.

[40] OpenCFD Ltd. at ESI group, OpenFOAM, The Open Source CFD Toolbox, User Guide; 2012.

[41] Deshpande SS, Anumolu L, Trujillo MF. Evaluating the performance of the two-phase flow solver interFoam. Comput Sci Disc 2012;5:014016.

[42] Rusche H. Computational fluid dynamics of dispersed two-phase flows at high phase fractions. Imperial college of science. London, UK: Technology & Medicine; 2002.

[43] Brackbill JU, Kothe DB, Zemach C. A continuum method for modeling surface tension. J Comput Phys 1992;100:335–54.

[44] Weller HG. Derivation, modelling and solution of the conditionally averaged two-phase equations. Technical report TR/HGW/02, Nabla Ltd; 2002.

[45] OpenCFD Ltd. at ESI group, OpenFOAM, The Open Source CFD Toolbox, Programmer's Guide; 2012.